

LA-UR-8/-838

Approved for public release;
distribution is unlimited.

c.1

Title: AHF Technical Status Report, January 2001

Author(s): P. Lisowski, J. McClelland, C. Morris, H. Thiessen, P. Walstrom, F. Neri, T. Wang, R. Little, M. Schulze, C. Mottershead, W. Lysenko, J. Waynert, J. Kelley, J. Zumbro, A. Jason, B. Blind, D. Barlow, P. Schwandt (IUCF), D. Friesel (ICUF), J. Schultz (MIT), B. Smith, (MIT), R. Camille (MIT), R. Myatt (MIT), A. Radovinsky (MIT), R. Thome (ex-MIT/GA), D. Johnson (SAIC), M. Wilson (K-Tech)

Submitted to: Distribution



Los Alamos

NATIONAL LABORATORY



Los Alamos National Laboratory, an affirmative action/equal opportunity employer, is operated by the University of California for the U.S. Department of Energy under contract W-7405-ENG-36. By acceptance of this article, the publisher recognizes that the U.S. Government retains a nonexclusive, royalty-free license to publish or reproduce the published form of this contribution, or to allow others to do so, for U.S. Government purposes. Los Alamos National Laboratory requests that the publisher identify this article as work performed under the auspices of the U.S. Department of Energy. Los Alamos National Laboratory strongly supports academic freedom and a researcher's right to publish; as an institution, however, the Laboratory does not endorse the viewpoint of a publication or guarantee its technical correctness.

1. An Advanced Hydrotest Facility for the Stockpile Stewardship Program

1.1. Introduction

By presidential and congressional direction, the US Department of Energy (DOE) has been made responsible for the safety, reliability, and performance of nuclear weapons without resorting to underground testing and for providing an infrastructure and intellectual capability to maintain the nuclear weapons stockpile.¹ This important work is done by the Stockpile Stewardship Program (SSP) through activities at the three DOE Defense Programs' weapons laboratories—Los Alamos National Laboratory (LANL), Lawrence Livermore National Laboratory (LLNL), and Sandia National Laboratories (SNL)—and production plants.²

To achieve the goals of the SSP, the United States has evolved from reliance on direct observation of underground nuclear testing to a science-based approach that seeks to develop a greater scientific understanding of nuclear weapons phenomena and better predictive models of performance. A key element of this approach is an improved simulation capability benchmarked by hydrodynamic tests, or hydrotests, and dynamic experiments using hydrodynamic radiography.

Hydrotests, using simulant materials in place of the fissile materials in an actual weapon, provide diagnostic information on the behavior of a nuclear weapons primary. These tests can be used to evaluate the effects of aging on the nuclear weapons remaining in the smaller stockpile. Dynamic experiments are used to gain information on the physical properties and dynamic behavior of materials used in nuclear weapons, including changes caused by aging. The integral information produced by these types of tests and experiments cannot be obtained in any other way.

For future stockpile certification, the integral performance of nuclear assemblies must be inferred with substantially improved fidelity over that currently possible. The Advanced Hydrotest Facility (AHF) will allow scientists to assess the changes in performance, reliability, and safety that will inevitably come with our maturing stockpile. Effects that we must be able to address will arise from aging components or remanufactured weapons and components. In addition, the AHF will provide a tool to assess potential terrorist-threat devices and mechanisms for their disablement.

1.2. Advanced Radiography

Hydrodynamic radiography refers to a technology used to view inside thick material objects as they are undergoing implosion and compression because of the detonation of surrounding high explosives. The principal tool of hydrotesting is thick-object-penetrating radiography. The images obtained must be formed very quickly, in 50 ns or less, to freeze the motion of the moving components and features and to avoid motion blur. The resulting images are negatives, in that the information depicting the primary assembly's internal structure is obtained from the attenuation of the penetrating radiation.

¹ National Defense Authorization Act (Public Law 103-160).

² Los Alamos National Laboratory, Los Alamos, NM; Lawrence Livermore National Laboratory, Livermore, CA; and Sandia National Laboratories, Albuquerque, NM.

Such radiographs were traditionally created using x-rays, but recent experiments have demonstrated that proton radiography is a more robust solution. In proton radiography, a high-energy beam of protons impinges directly on the object to be radiographed. Unlike x-rays, protons undergo a large number of very forward-angle scatterings as they pass through the object and the exit window of the containment vessel. This introduces a blur to the image that is then essentially removed by a recently developed magnetic lens system between the object and the detectors. The residual blurring can be further reduced by increasing the energy of the proton beam. For typical weapon-primary assemblies and containment-window thicknesses, sub-millimeter resolutions can be obtained with proton beam energies near 50 GeV, which can be produced in conventional accelerator architectures.

Protons have a number of advantages over x-rays in producing radiographic images. Protons have long, mean-free paths that are well matched for imaging thick, dense objects, and the proton results are sensitive to both material density and composition. The final images produced with protons also have a significantly higher signal-to-noise ratio than x-ray images. In addition, protons provide a high detection efficiency that can generate many frames and simultaneous view directions of the explosion, producing a kind of "motion picture." Proton radiography is also easier to execute. There is no need for a Bremsstrahlung converter (which is needed to produce x-rays by converting high-intensity electron beams) because the proton beam directly illuminates the object. And finally, proton accelerator technology already exists to provide the required beam energies, intensities, and time structures, making this technique a viable alternative for immediate application.

Proton radiography conveys several other distinct advantages. Because it uses magnetic lenses to focus the proton beam, the actual image can be as much as several hundred feet from the object itself. This is important because the setback substantially reduces the background noise from unwanted radiation. Because high-energy proton accelerators make a series of proton pulses that can be split and bent magnetically, measurements of an implosion can cover almost the entire duration of an event producing images at many angles simultaneously.

Confidence in the scientific basis of a proton-based AHF is the result of a series of events beginning in 1995 with development of lens systems to obtain images from transmitted high-energy proton beams. At that time, there had been no confirmatory measurements because there were no facilities in operation capable of performing dynamic experiments with sufficiently energetic protons. Following a technical contract developed by the Tri-Lab Working Group, it was agreed that a complementary set of measurements would provide confirmatory evidence that proton radiography would meet the needs of future stockpile certification. The complementary set includes:

- Dynamic measurements of *thin systems* that could be radiographed by medium-energy 800-MeV proton beams from the Los Alamos Neutron Science Center (LANSCE) accelerator,³ and
- Static measurements available at Brookhaven National Laboratory (BNL) of *thick systems* using high-energy proton beams with energies up to 24 GeV.⁴

³ N.S.P. King et al., "An 800-MeV Proton Radiography Facility for Dynamic Experiments," *Nucl. Instru. & Methods, A* 424 (1999) pp. 84-91.

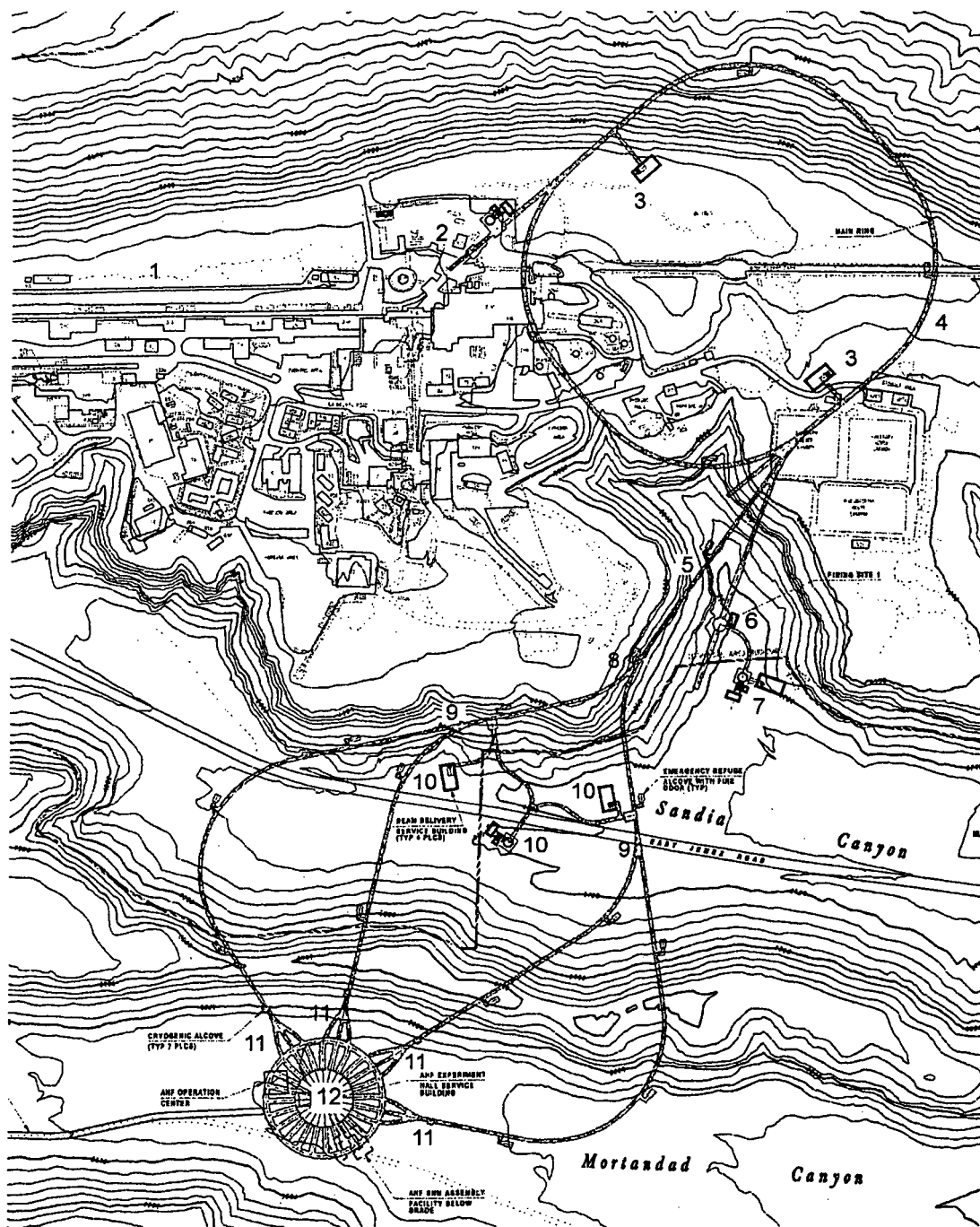
The confirmatory dynamic experiments validated the theory and simultaneously provided valuable information on the progression of burn fronts in high-explosive materials. They also demonstrated the unique ability of proton radiography to distinguish materials according to their density (i.e., atomic number). Although the first experiments produced a single frame per event, a fast sequence of pictures (a "movie") can eventually be obtained because a particle accelerator delivers a sequence of beam bursts short enough to freeze the motion of the object being radiographed. This movie capability was demonstrated at LANSCE in June 1999 by an American and British collaboration. In that test, a sequence of 11 frames was recorded.

1.3. System Description

Implementing a proton-radiography-based AHF requires construction of a 50-GeV low-repetition-rate synchrotron with operating parameters in the range of several existing machines. The synchrotron energy is determined by the need to have adequate resolution after the protons pass through the necessary multiple containment vessels to safely capture the products of the hydrotest. After extraction from the synchrotron using a fast kicker magnet, the beam is split into multiple beam lines and transported using DC and pulsed magnets. Up to 12 beam lines converge at the site of the experiment, each carrying 10^{11} protons per pulse, with all pulses in a single frame arriving within 50 ns. Each beamline has a diffuser and magnetic lenses to prepare the beam. After transmission through the test object, a multiple-element lens and detector system is used to produce the radiographic images.

The project is considering several different sites and configurations for an AHF. The major project systems are shown in Figure 1 for one possible configuration. Although no site has been selected, we have concentrated on an installation that can use the LANSCE 800-MeV proton accelerator as the injector. Depending on the synchrotron magnet choice, a small 3-GeV synchrotron may be needed between the LANSCE accelerator and the 50-GeV synchrotron to increase the proton intensity in order to provide full radiographic imaging capability with 12 views.

⁴ J. F. Amann et al., "High-Energy Test of Proton Radiography Concepts (U)," 11th Biennial Nuclear Explosives Design Physics Conference (NEDPC97), Livermore, California, October 24-24, 1997, Los Alamos National Laboratory report LA-UR-97-4721.



- | | | |
|--|----------------------|-----------------------------------|
| 1. LANSCE linac (elev. ~7,000 ft) | 5. Beam transport | 9. Routers magnets (2 total) |
| 2. Vertical injection | 6. Firing Site 1 | 10. Beam transport service bldgs. |
| 3. Power supply bldgs. (elev. ~6,900 ft) | 7. FS1 service bldg. | 11. Three-way splitters (4 total) |
| 4. Synchrotron (elev. 6,620 ft) | 8. Two-way splitter | 12. Firing Site 2 |

Figure 1. Twelve-axis, normal-conducting synchrotron and beam transport layout for AHF. This arrangement has an asynchronous beam transport in which pulses taking the outer path are extracted 900 ns before pulses taking the inner path to the multiple axis firing site.

The AHF is planned to be built in a way that allows the laboratories

- (1) to get data early in the project, and
- (2) to allow construction of additional capability while commissioning and operation of the accelerator at the initial firing site is underway.

The AHF Project will bring into operation a national user facility with the significantly increased radiographic capability required for future stockpile certification.

1.4. Technical Requirements

As a result of a careful consideration of overall functional requirements, a Tri-Lab Requirements Working Group derived a set of technical requirements in 1997 and in subsequent workshops. These requirements, in the context of current planning, are summarized as follows:

- The AHF must be able to first produce single-axis images of full-scale weapon implosions using surrogate material with 0.5- to 1-mm resolution.
- The system must be able to conduct full-scale hydrotests within special containment vessels that protect workers, the environment, and the public.
- The system must be able to produce a sequence of images, or frames, in a time that spans the progression of the event being observed. Beam bunches must have a short enough duration to freeze motion and must be timed so that a number of images can be observed while the event progresses with an axis-to-axis timing jitter of less than 50 ns. During the time of maximum compression, 10 pulses separated in time by approximately 200 ns are required.
- The beam must have sufficient protons to provide adequate information—approximately 1×10^{11} protons per frame per axis at 50 GeV, or, for 10 frames, 1×10^{12} protons per event per axis.
- There must be an upgrade to three-dimensional imaging using up to 12 axes with comparable resolution and pulse-train timing requirements. This will require a beam intensity of approximately 3×10^{13} protons per event.
- The facility must be capable of conducting dynamic experiments with plutonium. This capability must include multiple layers of protection for the public, workers, and the environment. It must include facilities for assembling these experiments.
- Resolution for dynamic experiments with plutonium experiments must be less than 1 mm.

Site evaluation and selection will take place in accordance with National Environmental Policy Act (NEPA) requirements during the conceptual design phase of the project and after a siting trade study has been completed. In addition to the LANSCE site discussed here, other potential sites at Los Alamos as well as different geographic locations will be considered.

The accelerators and firing sites for this study were located in tunnels mined into the volcanic tuff in the mesa below the LANSCE accelerator complex. If this site were chosen, the synchrotron would be approximately 350 ft below the mesa top. Beam tunnels to the second firing site would be at least 50 ft below the floor of the adjacent canyon, passing far enough

below a neighboring road to meet radiation safety requirements in the event of the worst-case beam-loss accident.

1.5. Project Activities

In FY1999, a small LANL-LLNL project team began compiling results of an earlier study of a synchrotron system planned to develop a single-axis capability. That work was summarized in an internal report.⁵ Beginning in FY2000 the project initiated a series of trade studies with multiple technical purposes but two main goals:

- Establish a path toward the most technically credible and cost-effective option for a conceptual design, and
- Examine and refine performance, cost, and schedule project risk in order to determine engineering development activities to mitigate those risks.⁶

Specifically, the studies identified four key areas for study given the available funding. They were:

- Synchrotron lattice design options and choice of magnets,
- beam transport and lens configurations and choice of technologies,
- power supply and electrical grid issues, and
- integration of the above studies with the conventional system framework needed to support the facility, including a firing site capable of safely supporting dynamic experiments with plutonium.

The trade studies refined the options available for further design and identified areas of project risk. A final decision has not been made on the most promising configuration pending completion of the design studies at alternative sites. Nevertheless, several important conclusions were drawn:

- Refining the synchrotron magnetic lattice beyond the earlier study was needed to attain the required pulse intensity,
- Building a normal-conducting synchrotron magnet based on a variant of the Fermi National Accelerator Laboratory (FNAL) Main Injector magnet would be a cost-effective, low-technical-risk approach,
- Designing a beam transport system using a kicker magnet to extract pulses from the synchrotron together with a router magnet in the transport system allows increased flexibility and reduce size and complexity,
- Superconducting quadrupole lenses are attractive to attain the high gradient over the large apertures required and to achieve a reasonable power consumption and to attain the necessary magnet focusing, and

⁵ P. Walstrom et al., "Draft Pre-Conceptual Design Report for the Advanced Hydrodynamics Facility," Vol. 1., Los Alamos National Laboratory report LA-UR-99-4421, October 1999.

⁶ D. Barlow et al., "Advanced Hydrotest Facility FY2000 Trade Study Report," Los Alamos National Laboratory report LA-CP-00-379, September 2000.

- The grid can serve electrical power requirements for an AHF at Los Alamos directly if variants of the FNAL magnets or superconducting magnets are used in the transport line. Alternative energy-storage devices suitable for powering the AHF are available should the grid prove unsuitable.

The trade studies reaffirmed earlier conclusions that a proton-based AHF can be built to meet mission requirements. Areas identified as needing engineering more work include the development of a suitable kicker extractor modulator, developing a superconducting quadrupole lens, choosing and prototyping synchrotron and transport magnets, and developing an approach for use of composite vessels within which to safely conduct dynamic experiments with plutonium.

During FY2001 the project team will continue to grow in size with \$15 million in funding from the DOE. The project will begin detailed investigation of the required experimental program for the facility, and will undertake a study to further refine the details of the multi-axis firing site capable of performing dynamic experiments with plutonium.

2. Proton Radiography Development

A research and development program to demonstrate proton radiography as the leading technology for the AHF is nearly complete. The program was constructed around a set of critical issues relating to radiographic requirements for the AHF and reviewed by an external advisory committee (EAC). In addition to 50-GeV protons, several-mega-electronvolt x-ray sources driven by linear induction accelerators and inductive voltage adders are also being evaluated. The EAC was appointed by LANL, LLNL, and SNL and charged to comment on the appropriateness of the R&D program, review progress and issues, and make recommendations on a technology down-select.

Because an actual proton hydrotest facility does not currently exist, the R&D plan includes a combination of dynamic-object (explosively driven) experiments at LANSCE, using 800-MeV protons, and static object experiments at 25-GeV at BNL's Alternating-Gradient Synchrotron (AGS).

2.1. Proton Radiography at LANSCE

LANSCE is capable of providing 800-MeV protons, which are well suited for examining shock-wave propagation in small-scale, high-explosive systems. This lower energy limits the sample candidates to relatively thin, low-Z systems. These limitations arise primarily from multiple scattering and energy loss within the object and aberrations in the lens system, effects that become less important as the beam energy increases. The LANSCE proton radiography facility includes a beam transport system to match the input beam onto the object, a steel vessel to contain the high explosives (currently limited to 750 g of high explosives, but upgrades in the near future will raise the limit to 4.5 kg), a two-lens magnetic transport and collimation system to perform material sensitivity experiments, and a multi-framing detector system capable of capturing up to 14 images at 11 different times on a single shot (to be upgraded to 16 frames). Future detector development is expected to provide the ability to take thousands of frames during the explosion to produce a more detailed motion picture of the event. More than 70 dynamic shots have been performed at LANSCE since 1997. These experiments typically look at shock behaviors within the high explosive or shocked materials properties.

2.2. High-Energy Proton Radiography at Brookhaven National Laboratory

In addition to our work at LANSCE, we have been conducting static experiments using high-energy protons (up to 25 GeV) at BNL's AGS. The AGS offers a high-energy test bed for proton radiography that is close to AHF beam parameters. This work is described below in Section 3.

2.3. Other Uses of Proton Radiography

The applications of proton radiography are not limited to SSP activities. It can also be used to produce radiographic "movies" to study basic materials properties under dynamic conditions, such as spall, ejecta, crack formation and propagation, and shock physics. Industrial applications include diagnosing performance of internal combustion engines, jet turbines, and structural failure analysis. We are currently working with a major automobile manufacturer who is interested in investigating a wide range of engine component evaluations under dynamic conditions using proton radiography, including cooling system flows, combustion dynamics, piston ring action, and critical dimensional changes induced by engine internal forces as it

operates. Proton radiography offers unique advantages in these applications. Another major automobile manufacturer has also expressed interest in these techniques, along with various turbine and jet engine manufacturers.

3. Proton Radiography

3.1. Introduction

In transmission radiography, the transmitted flux through an object is used to measure its areal density. The transmission, t_λ , is given in terms of the path length l through the object and mean free path λ by:

$$t_\lambda = e^{-l/\lambda} \quad (1)$$

This is measured as a function of position and inverted to calculate the thickness of the object as:

$$l = -\lambda \ln(t_\lambda) \quad (2)$$

Here, λ is given by

$$\lambda = \frac{1}{\rho\sigma}. \quad (3)$$

A simple model for proton radiography can be obtained by assuming the nuclear scattering results in the removal of beam particles from the transmitted flux described by Eq. (1) and that Coulomb scattering can be approximated by assuming transmitted particles are scattered into a Gaussian-shaped angular distribution. In this approximation, integration of the angular distribution between limits imposed by angle collimators at the Fourier points in the lenses results in closed-form expressions for the transmission.⁷ A beam transmitted through an object acquires the angular spread

$$I(\theta) = \frac{1}{\pi\theta_0} e^{(-\theta^2/2\theta_0^2)}, \quad (4)$$

where

$$\theta_0 = \frac{14.1}{p\beta} \sum_i \frac{\rho A_i}{X_i}. \quad (5)$$

Here p is the beam momentum, $\beta = v/c$, where v is the beam velocity and c is the speed of light; X_i is the radiation length for the i 'th material. Throughout the rest of this work the sum will be implied. This can be integrated between angular limits, θ_1 and θ_2 ,

$$\int_{\theta_1}^{\theta_2} I(\theta) \sin(\theta) d\theta d\varphi = e^{-(X_2/\rho_x)} - e^{-(X_1/\rho_x)}, \quad (6)$$

where

$$\rho_x = \sum_i \frac{\rho A_i}{X_i}$$

⁷ N.S.P. King et al., "An 800-MeV Proton Radiography Facility for Dynamic Experiments," *Nucl. Instru. & Methods*, A 424, pp. 84-91, March 11, 1999.

is the areal density of an object, and

$$X_1 = p^2 \theta_1^2 / (2 \times 14.1^2),$$

with a characteristic areal density associated with the small polar angle limit, θ_1 , and

$$X_1 = p^2 \theta_2^2 / (2 \times 14.1^2),$$

with a characteristic areal density associated with the small polar angle limit, θ_2 .

Multiple lenses on a single axis, with different angular collimators, allow Coulomb radiation lengths to be separated from nuclear attenuation lengths in proton radiography. Transmission through a single lens, including both nuclear and Coulomb attenuation, is given by

$$I = e^{-\rho_\lambda} \left(e^{-(X_2/\rho_\lambda)} - e^{-(X_1/\rho_\lambda)} \right). \quad (7)$$

The most precision can be obtained with a set of two lenses, where the first is optimized to measure only nuclear attenuation by having a large aperture. If the small angle cut is zero and the large angle limit is large enough so that second term can be ignored, transmission through the first lens in a two-lens system is

$$I_1 = e^{-\rho_\lambda}. \quad (8)$$

If the second lens has a large, large angle limit, but does have a small angle cut (Fermi collimator)⁸ then transmission through the second lens is given by

$$I_2 = e^{-\rho_\lambda - (X_2/\rho_\lambda)}. \quad (9)$$

Equations (5) and (6) can be solved for the nuclear-attenuation-length-weighted areal densities

$$\rho_\lambda = \ln(I_1), \quad (10)$$

and the radiation-length-weighted areal densities

$$\rho_\lambda = \frac{1}{\ln(I_1) - \ln(I_2)}. \quad (11)$$

In 1996, we performed the first proton radiography experiment at the AGS using a secondary beam of 7- to 10-GeV protons at low intensity. The lower intensity prevented us from performing true flash radiography, but the resulting data were able to demonstrate the low background level at the detector, confirm calculations of system performance, and prove the utility of the magnetic-lens system at high energies.

To achieve a true flash radiograph of a static object, we constructed a new beam line at the AGS to deliver the full energy of the accelerator (25 GeV) at full AHF intensities (10^{11} protons per pulse). This beamline included two sets of lenses to allow for the determination of material composition as well densities. An experiment was run on this new beamline in 1999 with the

⁸ C. L. Morris, Eric Ferm, Nick King, Mary Hockaday, Gary Hogan, Kevin Morley, Alexander Saunders, and John Zumbro, "A comparison of collimators and anti collimators for multiple scattering radiography," Los Alamos National Laboratory report LA-UR-00-2934 (2000).

goal of demonstrating position resolutions, mass, and material sensitivities at the levels needed to meet the AHF requirements on a thick object. Preliminary analysis of the data underway at LANL and LLNL indicates that these objectives were met. Limitations imposed by the existing magnets in the beamline prevented a full demonstration of material identification on thick objects, however. The lens system is now being upgraded and another run is planned for January of 2001. We will also perform tomographic experiments by rotating and imaging a three-dimensional object in the beamline to provide information on the numbers and orientations of axes needed for the AHF. We will also continue detector development, shielding studies, and beam tailoring to further reduce backgrounds at the image plane.

In this report we present data from Experiment 933, which was recently completed at BNL and demonstrates many of the features of proton radiography. A matching section and two lenses were constructed using existing refurbished 8Q48 quadrupole magnets in Line U at the AGS. This system was installed and commissioned using single pulses of up to 10^{11} protons at 24 GeV/c provided by the AGS. The pulse intensity was administratively limited to this value by AGS safety requirements. A picture looking upstream from the end of the second lens is shown in Fig. 2.



Figure 2. A view of the Experiment 933 setup looking upstream from the first camera location. The active cameras can be seen in the middle of the photograph.

Diagnostic data were obtained on a pulse-by-pulse basis with transformers, which measured proton fluxes at three locations in the beamline: upstream of the diffuser location, and at each of the down image locations downstream. The beam position and angle at the diffuser location were monitored using two CCD cameras looking at two phosphors: one mounted on the diffuser and one located approximately 6 in. upstream of the diffuser. Combining the data from these measurements in principle allows accurate pixel-to-pixel normalization of transmitted flux through an object to be obtained by normalizing to the measured fluxes and correcting the beam

profile for shifts in position, which was measured using the upstream images. Although preliminary analysis of the upstream data shows a correlation with the downstream beam spot location, this information was not used in the remaining analysis.⁹ Since a similar system would have a large impact on AHF costs by removing much of the need for an upstream lens in the matching region, more work on this problem is needed.

The matching lens was tuned by removing the downstream collimator and installing a phosphor and CCD camera system at the collimator location. The beam was centered on the phosphor by steering it at the diffuser location, and the spot was minimized by adjusting the matching quadrupoles. One of the matching magnet power supplies was run near the top of its range. The size of the beam at the collimator location corresponded to about 0.5 mrad of angle resolution at the object location. This size, which is related to the emittance of the accelerator, puts a scale on the thinnest objects that can be radiographed. The 0.5 mrad-measured resolution corresponds to about 0.85 radiation lengths, or about 6 mm of tungsten. This is radiographically equivalent to having a uniform fixed amount of material in addition to any other object that is in the beam. A diffuse halo amounting to about 4% of the total beam intensity was observed. Beam pictures and lineouts at the collimator location are shown in Fig. 3. The beam emittance can be accounted for radiographically by including it in the transmission.

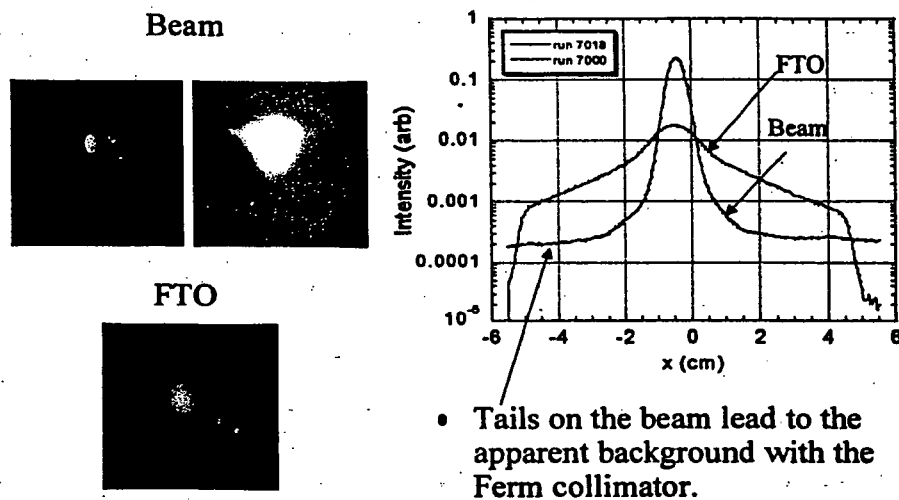


Figure 3. Images of the beam taken at the collimator location are shown on the left. The top two images are taken with nothing in the beam, and the low image is with the FTO in the beam. Lineouts are displayed on the right. The right beam image is displayed with an expanded z scale to show the tail.

3.2. Background Measurements

After tuning both the matching magnets and the lens focal length, a 1-mrad collimator was installed in the upstream lens, a 1-cm diameter, 15-cm-long tungsten rod was mounted at the object location at the beginning of the first lens, and images were made with and without the FTO mounted in the object location of the second lens. The tungsten rod produces a hole in

⁹ Ed Hartouni, Talk presented to an Experiment 933 collaboration meeting.

the beam downstream of the first lens. The background produced by each of the collimators was measured by studying how much this is filled in when an object is put in the beam with the collimator mounted in the downstream lens. The backgrounds measured from the 4.4- and 3-mrad normal and 3-mrad Fermi collimators were 2.1, 3.9, and 4.6% at the limb of the FTO, respectively. Although these are somewhat higher than simulations predict, they are low enough to be easily dealt with. Some of these results are displayed in Fig. 4.

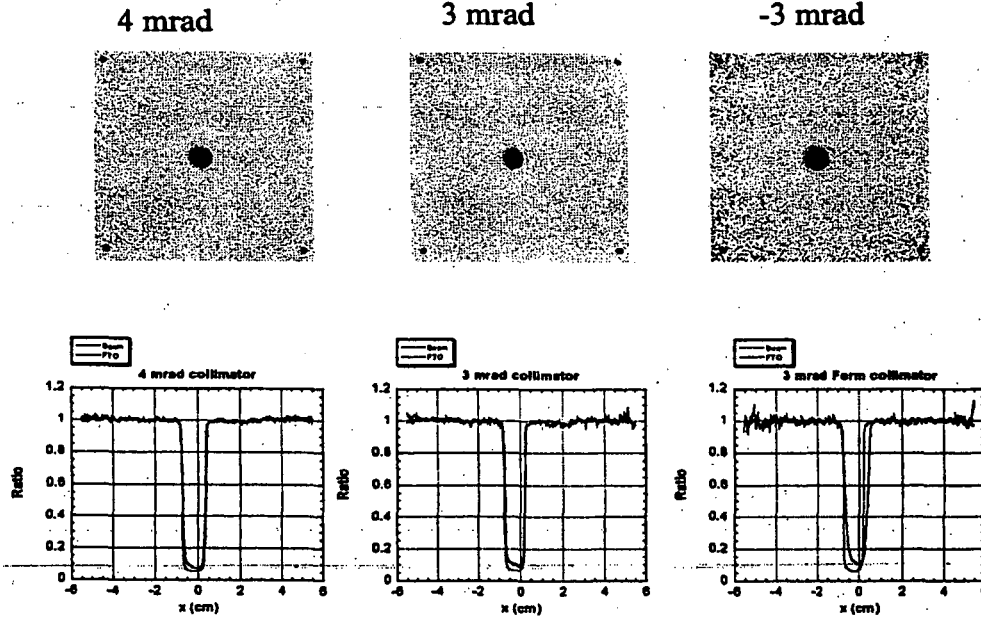


Figure 4. Top: Ratios of radiographs of the FTO with the shadow bar in to the shadow bar out for each of the collimators. Bottom: Lineouts of the beam ratioed imaged with the shadow bar in and the FTO-in in blue and with the FTO-out in red.

3.3. Position Resolution and Metrology

Position resolution and accurate metrology are important parameters for AHF applications of proton radiography. Quantitative measures of both of these parameters were obtained during Experiment 933.¹⁰

The magnetic optics in the beam line and the photon optics in the detectors potentially introduce geometric distortions. These can be measured using a fiducial grid plate, shown in Fig. 5. The fiducial plate places a uniform grid of features across the entire field of view. In the acquired data, the positions of these features can be used to measure geometric distortions.

¹⁰ A more complete description of some the test objects used during Experiment 933 can be found in Peter Barnes, "Test Objects for Calibrating the FTO as part of BNL E933," distributed to the collaboration, 1999.

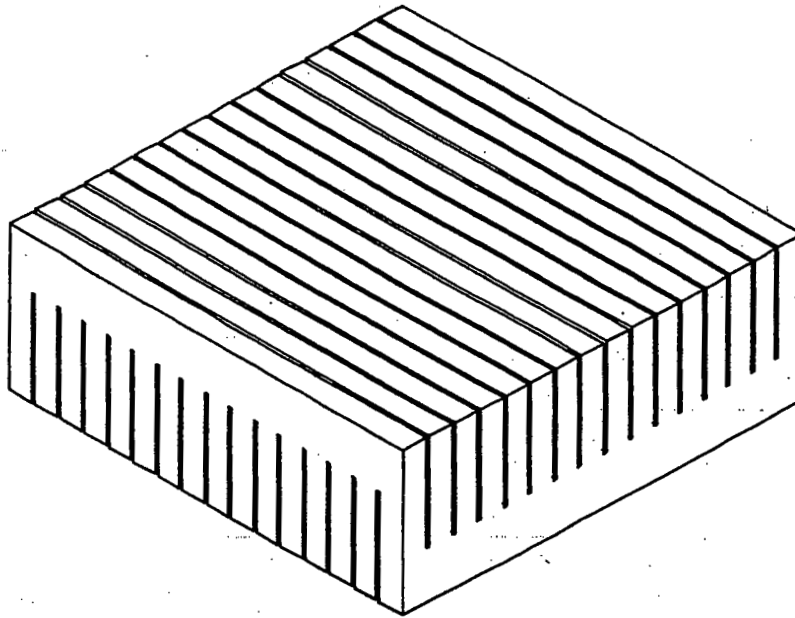


Figure 5. Fiducial grid plate. The plate is 3 in. thick, with perpendicular slots 2 in. deep cut into both faces. Each slot in the top face intersects each slot in the bottom face, forming a regular grid of square holes through the entire block.

A radiograph of this object is shown in Fig. 6. The expected structure is clearly visible. The data have been divided by a beam image, and the position scale was offset and adjusted with a rotation and linear scaling in both x and y . The residuals for all of the intersections are plotted in the figure. Some evidence for geometric aberrations can be seen in the residual plots. The rms position error average across the entire field of view is less than $100\text{ }\mu\text{m}$, with the largest contribution coming from the corners, where geometric aberrations are the largest.

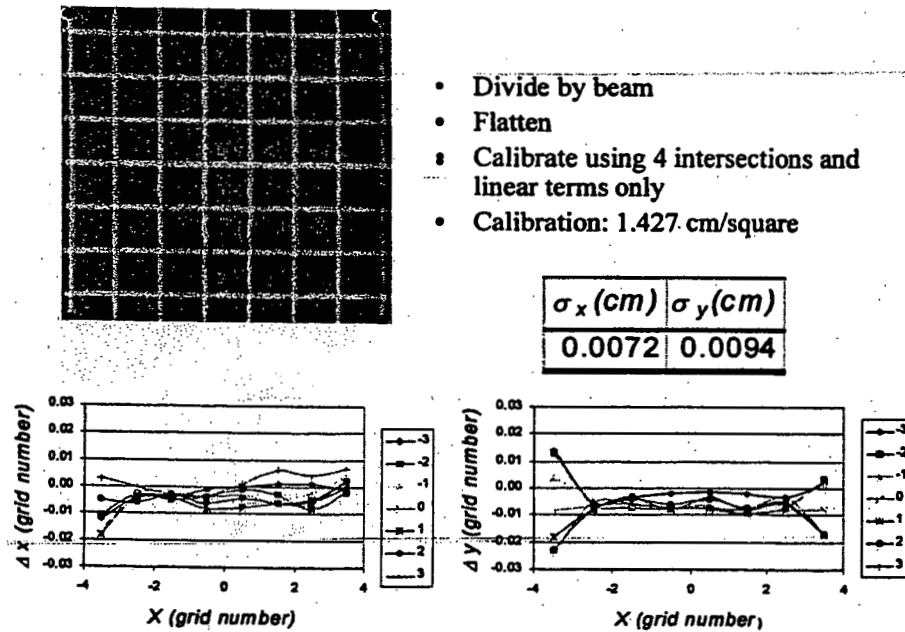


Figure 6. Radiograph and position residuals from the fiducial plate test.

Position resolution was measured using a resolution pattern machined into a 2.5-mm-thick piece of platinum, in both image planes. These data are shown in Fig. 7. The position resolution was measured to be 250 μm FWHM in the first image plane. A similar value was obtained in thicker classified test objects.

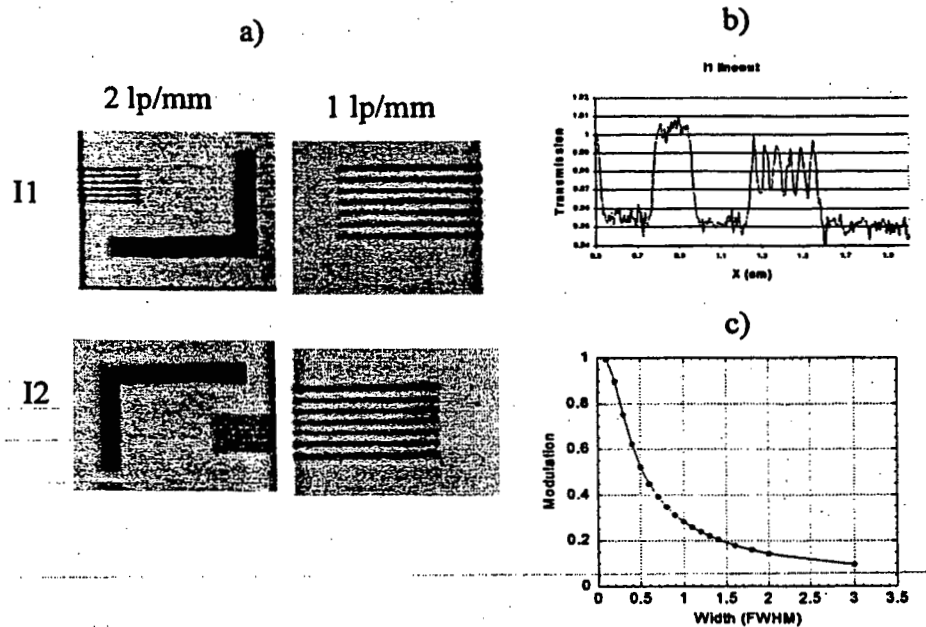


Figure 7. (a) Radiographs of the resolution test pattern. (b) Lineout of the two-line pair/mm test pattern from the image location 1. (c) Plot of the relationship between modulation and resolution.

3.4. Step-Wedge Measurements

After completing the lens characterization, a set of step-wedge measurements was completed on tungsten, copper, carbon, and Lucite, in order to provide cross sections to be used in quantitative analysis of other test objects. The finite acceptance of the beamline as a function of energy loss and scattering angle in an object can be expressed as an effective cross section, which must be known to reconstruct the density of an object from its radiograph. A simple way to measure the effective cross sections over the range of interest is to use a set of step wedges constructed from the same materials as the object and that span the thickness range of the object.

Figure 8 illustrates the step wedges used in Experiment 933. This design using two wedges back to back allows us to make a new configuration, a pair of wedges with small steps separated by a spacer block of the same material. This allows us to make the measurement on steps that differ by a small amount across a large range of total thickness, using only one pair of wedges. The approximate midplane symmetry simplifies alignment along the beam direction, and arranging the thickest part of the wedge to be in the center of the beam provides a better match of attenuation to the flux, optimizing the statistical precision of the cross section measurement for a given proton flux. Detailed descriptions of the actual step wedges used can be found in Ref. 7.

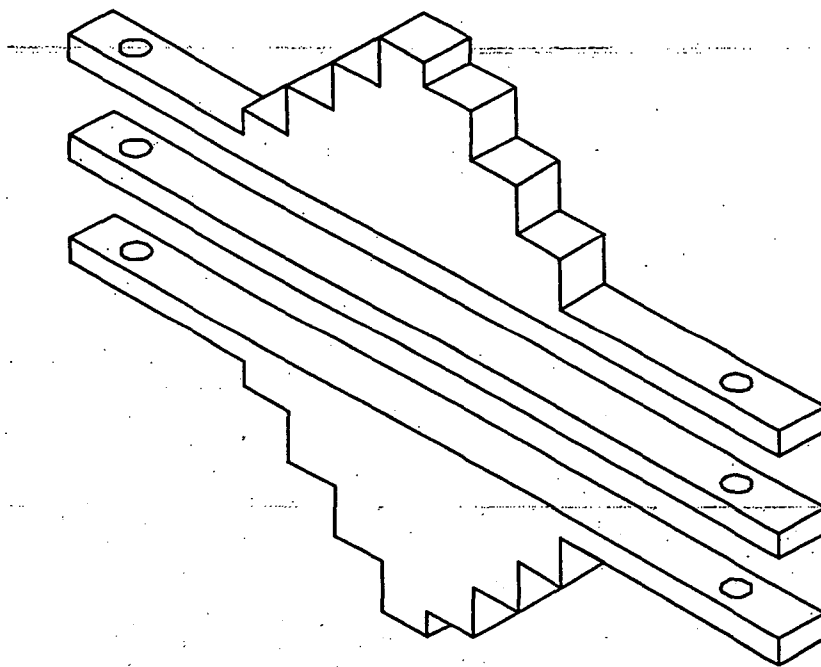


Figure 8. Doubly symmetrized step wedge. The thickness of the steps decreases on either side of center, more or less following the incident beam intensity. Using a pair of half-height wedges back to back keeps the center at a constant position, and allows the insertion of spacer plates of the same material.

The steps in the analysis of the step-wedge data were to first align and average each of the four images plates exposed in each image plane for each picture. Four image plates were used to increase the DQE. Estimates made by comparing actual images with simulations suggested the resulting DQE was in the range of 20-40%. The data from image location one (I1) were divided by a smoothed beam image. The results were "flattened" by fitting a two-dimensional

polynomial to the regions of the picture where there was no material in the beam and then dividing the image by this polynomial. This helps to remove artifacts due to beam motion and non-uniform response of the image plates. The data from image location 2 (I2) were taken with a Fermi collimator. These data were rotated to account for the inversion of the lens, aligned with the images from image location 1 (I1), and then divided by the I1 results. The procedure for IL1 is illustrated in Fig. 9.

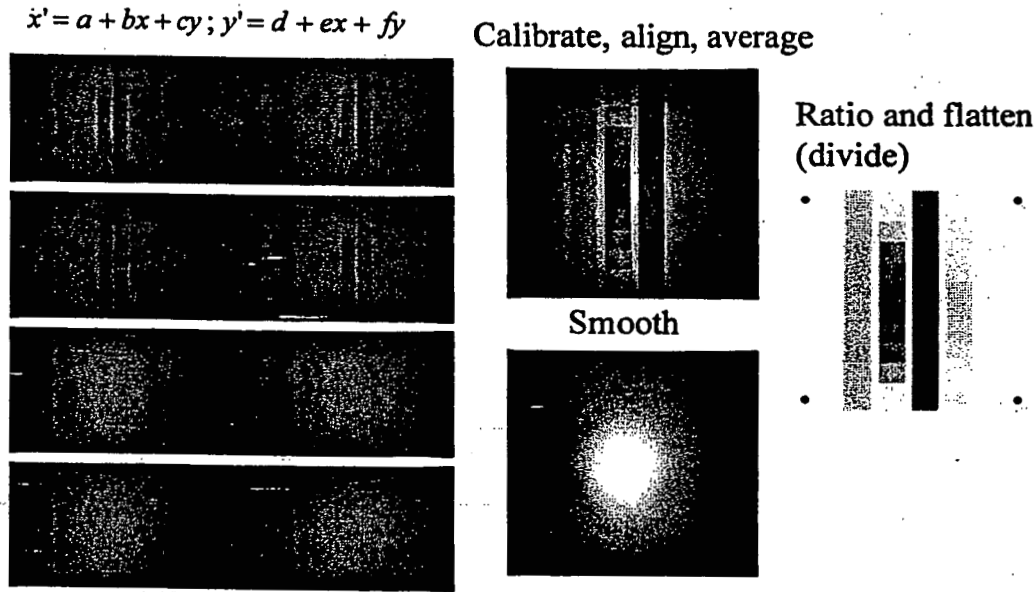


Figure 9. Images from the various steps in the analysis procedure.

Cross sections were measured in steps of 1% of an attenuation length up to the full thickness of the FTO for each of the materials. Some of the results for the 10% step wedge are shown in Fig. 10. The fit demonstrates the quality of quantitative agreement obtained between a semi-empirical model and the data. Step-wedge data were also taken looking through an additional 345 gm/cm² of tungsten. These data illustrate the capability of proton radiography to obtain quantitative data over an extremely wide dynamic range of object thickness. The full set of data for I1 for the tungsten step wedge is shown in Fig. 11.

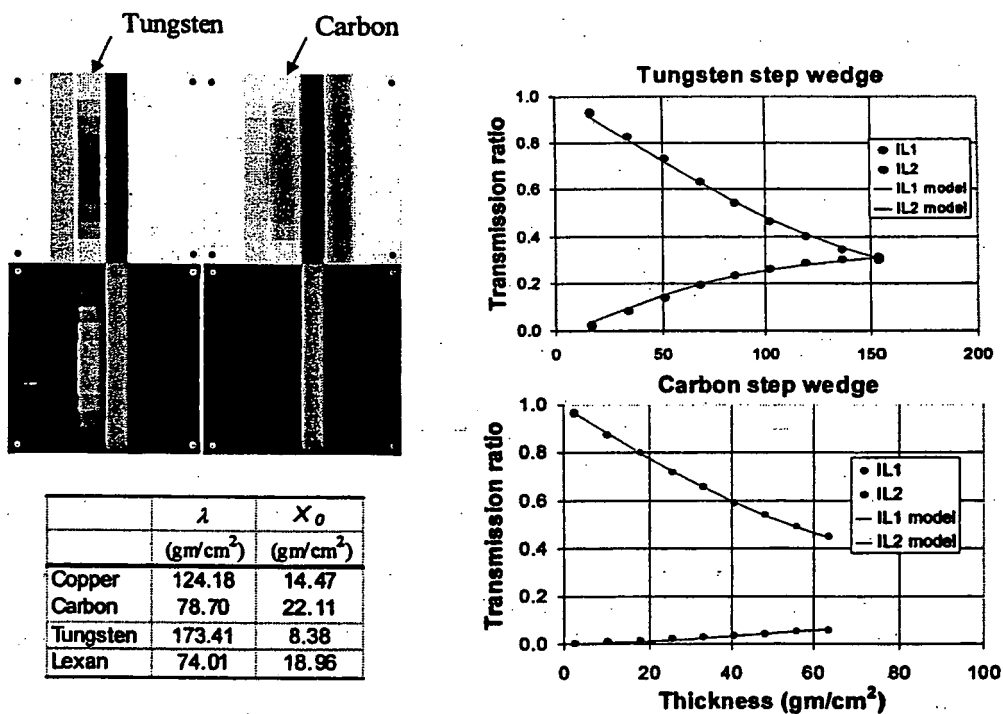


Figure 10. The carbon and tungsten 10% step wedge data.

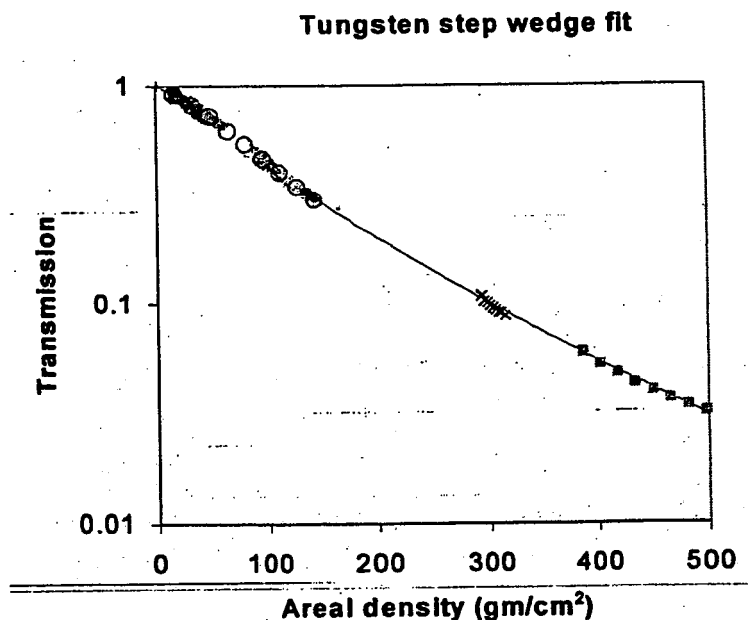


Figure 11. Image location 1 of tungsten step wedge data set. The line is a fit to the data that are used in the FTO analysis.

The data in Fig. 10 demonstrate the potential for material identification. The step wedges have been designed to cover a similar thickness range in nuclear attenuation lengths, but they have a much different thickness in Coulomb radiation lengths, with the tungsten being much thicker than the carbon in radiation length units. This results in much more multiple scattering in the

tungsten than in the carbon. Because of this, there is a dramatic difference in the 12 images, where the tungsten step wedge is clearly visible and the carbon is difficult to discern.

For thin objects, Eqs. (10) and (11) apply. This can be seen below where the functions of the transmission given by Eqs. (10) and (11) are plotted for the various 10% step wedges. The slope of these curves, which should be a measure of material type, can be seen to display the expected material dependence.

The tungsten step wedge, data span a wide range of thickness. A fit to the entire data set, assuming a Gaussian multiple scattering angular distribution and a Gaussian beam emittance, is shown as the solid line in the figure. The function form fitted to the flattened transmission is

$$I = e^{-\rho \lambda} \left[\frac{(1 - e^{-(X_1 / \rho_s + \rho \text{ fixed})})}{(1 - e^{-(X_1 / \rho \text{ fixed})})} \right] \quad (12)$$

The offset, $\rho \text{ fixed}$, has been added to account for the finite beam emittance. The denominator has been added to account for the flattening, which forces the transmission to be one of zero thickness, even though there is some attenuation due to the beam emittance. This function can be seen to give a good account of the data over a very wide range in step-wedge thickness. The fixed offset is also the reason for the non-zero intercept of the curves in Fig. 12.

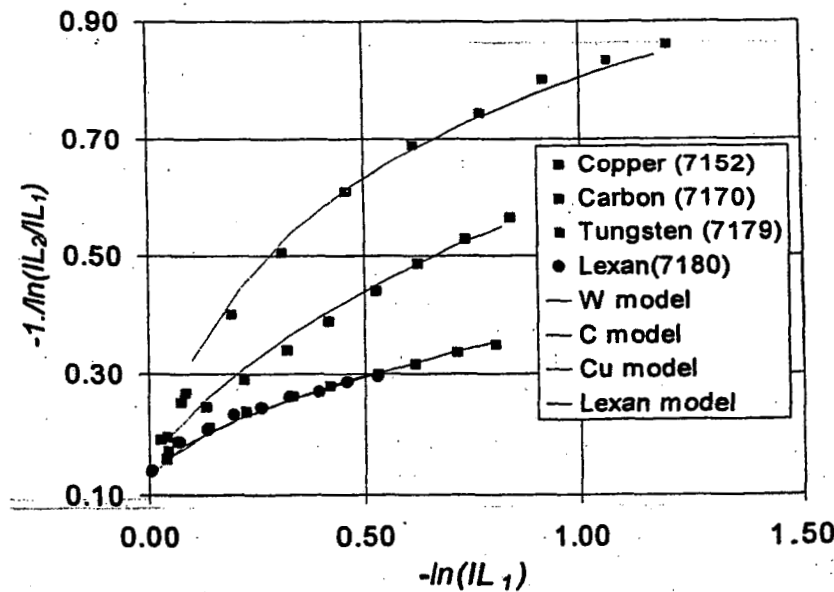


Figure 12. Plot of the functions of the transmission suggested by Eqs. (10) and (11) to demonstrate material identification. The materials in the step wedges are clearly distinguished.

The approximations in Eq. (12) do not work well for low-Z thin objects because of the long tails on the beam that can be observed in Fig. 3. This can also be seen by the departure from linearity for thin objects in Fig. 12. The small amount of multiple scattering introduced by the low-Z step wedges results in exaggerated attenuation when it is convoluted with the tails on the beam distribution. Nevertheless, the materials in the step wedges are clearly distinguished by different slopes. The effect of the angle cut in the first lens leads to the departure from linearity for the thicker steps of tungsten step wedge for which the multiple-scattering cone does not fit within the lens acceptance.

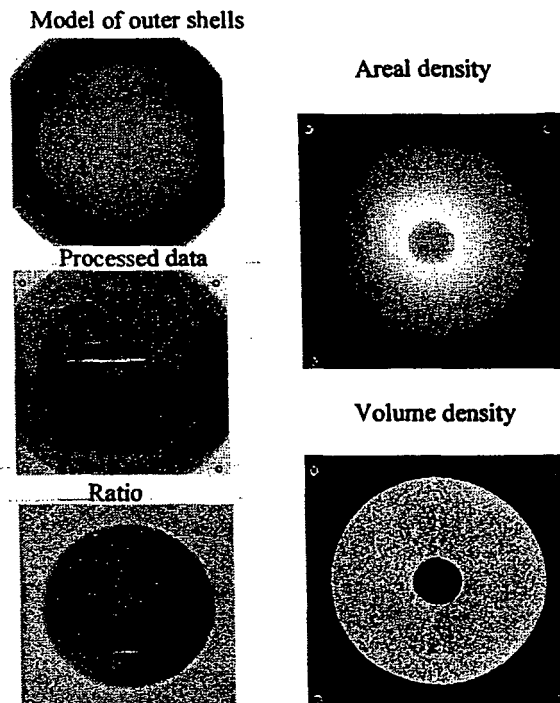


Figure 13. Top left: Model of outer shells. Middle left: measured transmission data. Bottom left: measured data divided by the model. Right top: Tungsten areal density. Right bottom: volume density.

3.5. Quantitative Density Analysis

The tungsten densities from the FTO have been reconstructed by using the data analysis procedures similar to those outlined in the step-wedge analysis. After the four image plates were averaged, the results were divided by model radiographs of the outer foam-and-copper shells (Fig. 13), and then the flattening procedure was applied to the region of the radiograph outside of the tungsten region. The resulting transmission image was transformed from transmission to areal density using the same procedure as was used in the step-wedge analysis but being careful to take into account the overlying material, including the outer copper-and-foam shells of the FTO. The resultant areal density image was centered and volume densities were calculated using a conditioned Abel inversion method described previously.⁵

The resultant volume densities can be compared with the measured tungsten density of $18.28 \pm 0.07 \text{ gm/cm}^3$. A histogram of the densities measured on $(169 \text{ } \mu\text{m})^3$ voxels in the region of the tungsten is shown in Fig. 14. The agreement between radiographic density and that obtained from metrology is robust and precise at the level of a percent or so. The AHF goal, driven by the criticality requirement, is to measure densities to 1-2% in absolute precision. This result meets that goal for the simple geometry of the FTO.

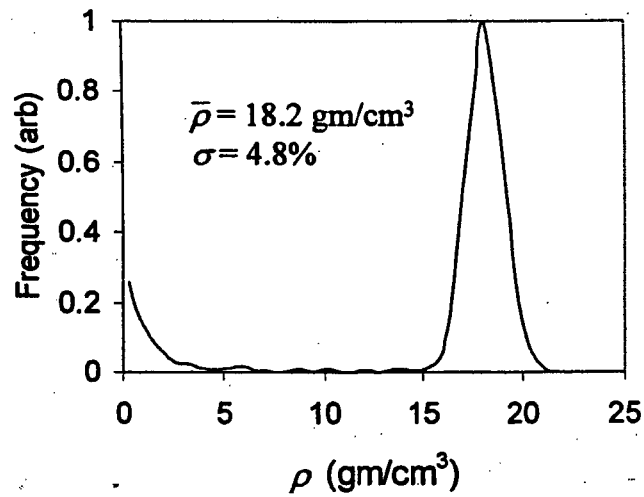


Figure 14. A histogram of radiographically measured densities in the tungsten region of the FTO. The mean value and the width are given in the figure.

3.6. Edge Resolution

The half-density contour for both the inner edge and the outer edge of the FTO has been extracted and analyzed to determine the precision with which edges can be extracted from high-energy proton radiography. The AHF requirement for this quantity is 75 μm . The radius for each of the x-y pairs was extracted from the contours, and then the mean and standard deviation of these was calculated. There was no constraint on the radius of curvature and no additional smoothing beyond that from the conditioned Abel inversion. This analysis provides an unbiased estimate of the precision with which radii can be extracted. Limits to the precision are due to the statistical accuracy of the reconstruction (the exposure of 10^{10} protons) and by systematic sources of error, such as magnetic aberrations. The contours are displayed as the red lines in Fig. 15.

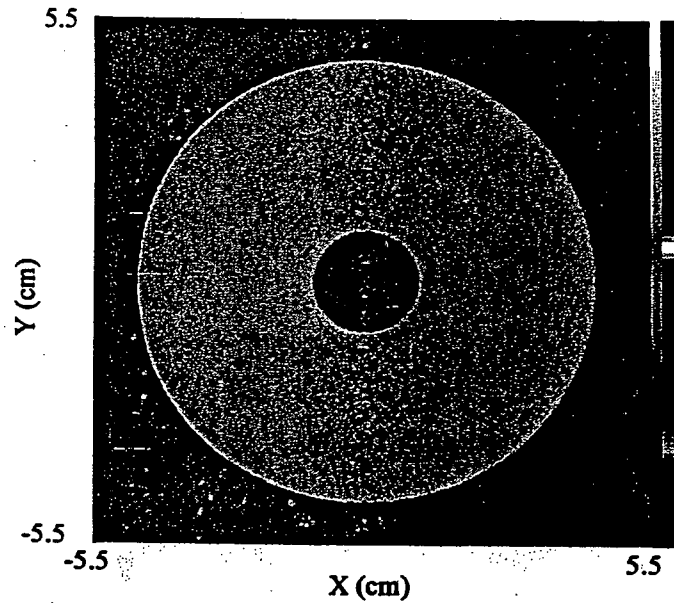


Figure 15. The red line shows the result of the contour finding routine on the volume density image from the FTO tungsten reconstruction.

The difference between the radii of the extracted contour and the average radius are plotted as a function of x in Fig. 16 for both the inner radius and the outer radius. Also shown in the figure are the mean and the standard deviations averaged over the entire contour.

The average values for the measured outer and inner radii of 4.494 and 1.014 agree well with the known dimensions of the object, of 4.500 and 1.000 cm, respectively. However, systematic discrepancies clearly dominate the residuals. This can be seen in Fig. 16 as the large correlation between the residual and x position. The random fluctuations, which are a measure of the statistical uncertainty and which impose the ultimate limit to the precision of edge determination, contribute about 30 μm to the total RMS.

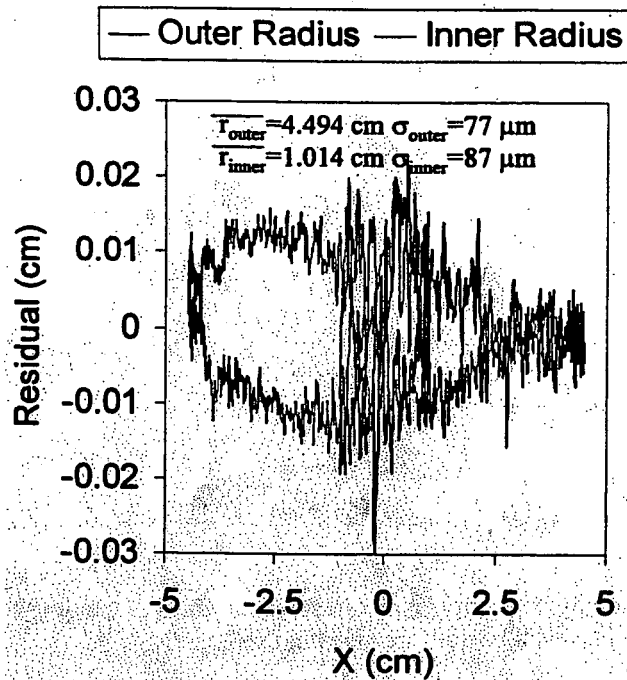


Figure 16. The residual (difference between the radius of the contour and the average radius) for the outer edge of the FTO in blue and the inner edge of the FTO in red.

3.7. Test Object Measurements

Following this sequence of lens setup and radiographic calibration experiments, data were taken on a wide range of test objects. Some of these experiments allowed direct comparisons with DARHT, FXR and Microtron x-radiography measurements. The dynamic range and sensitivity of flash proton radiography were demonstrated to exceed both the current state of either flash or fixed target x-radiography in the qualitative results of all of these experiments.

3.8. Conclusions

Some strong conclusions can be drawn from the current analysis of data. The quality of radiography necessary to meet, or nearly meet, the AHF goals for position resolution, density precision, timing, and sensitivity to small density changes has been demonstrated with protons. Concerns about background and dynamic range should be laid to rest. Material identification has been demonstrated. The ability to measure the size and amplitude of the incident beam has been demonstrated. Active cameras operating at DQEs in the tens of percent have been demonstrated.

4. Synchrotron Issues for Proton Radiography

4.1. Introduction

The pulse format of a proton synchrotron (high instantaneous intensity, multiple short-duration bunches, low average duty cycle) is ideally matched to the requirements of dynamic proton radiography. The energy of the AHF synchrotron is 50 GeV, which is the result of a compromise between improved performance and increased cost, with increasing energy. The other basic machine performance requirements are to provide at least 3×10^{13} protons per machine cycle, a bunch number of 24-48, and a cycle repetition time of 100 s. All of these requirements are well within the state of the art of proton synchrotrons. The phase-space requirements for the output beam are also not demanding. The only unusual requirements is for flexible single-pulse extraction scheme to use the bunches in a single machine cycle to provide a multi-frame, multi-view motion picture over a total time of tens of microseconds. Because the radiographic requirements only loosely define the synchrotron, an important part of the task of the AHF design team is to translate the radiographic requirements into facility requirements that are sufficiently defined so that engineering decisions can be made. Cost minimization requires some care in the choice of magnets and power-supply systems. Below we will describe constraints and proposed solutions for a 50-GeV proton synchrotron to be located at Los Alamos for proton-radiography applications.

In Table 1, we list the synchrotron specifications that have direct consequences for radiography. The main point to notice is that there are a few details of the synchrotron that are clearly defined by the requirements. Among these are:

1. The spatial resolution, which defines the minimum beam energy if a particular confinement system design is assumed;
2. The density resolution, which determines the number of protons needed per frame per axis (the total count of protons in the ring must be sufficient to service the entire facility with sufficient statistical accuracy in each frame);
3. The number of frames and pulse pattern available (so far, only a minimum number of consecutive frames (≥ 10) has been clearly defined), with an unclear need for some "early" pulses (up to 75 μ s earlier);
4. The minimum pulse spacing (the 200 ns assumed here is only roughly defined in the radiographic requirements documentation).
5. The repetition time must not be so long that radiographic experiments and detector calibration, etc. are hindered.

These requirements are insufficient to fully define a synchrotron.

Table 1. Synchrotron Specifications of Importance to Radiography

	1999 and earlier	Change in 2000
Resolution	0.5-1 mm	No change
Protons/frame/axis at diffuser	5×10^{10} to 1×10^{11}	1×10^{11}
Number of consecutive frames	≥ 10	No Change
Minimum pulse spacing	200 ns	200 ns
Time range (maximum)	75 μ s	75 μ s

	1999 and earlier	Change in 2000
Number of axes	8	12
Repetition time	10 s	Up to 100 s

The synchrotron design team, in cooperation with the LANL's P-Division radiographic team, has made a number of additional design assumptions in order to provide a fully defined facility design that is consistent with the radiographic requirements, minimize the estimated facility construction cost, and, at the same time, provide a set of specifications that is stable against parameter changes that are within the range of the precision of definition of the requirements. There are four major additional assumptions that are needed to proceed with the design. These assumptions are basic to the design of the facility as proposed and should be changed only if clear need for such a change is demonstrated in the radiographic requirements.

First among these design assumptions is the beam energy of 50 GeV. This energy is sufficient to achieve the desired resolution in through 1-in.-thick steel confinement vessel without windows, with better resolution available if a composite system is developed. Slightly worse resolution will be obtained should an armored liner or external safety vessel be required in addition to a 1-in.-thick steel confinement vessel. The second assumption is that a 797-MeV H^- beam is available for injection of the synchrotron. This allows a single-stage synchrotron with iron-dominated magnets to deliver the required maximum energy beam. For example, should a final beam energy of 100 GeV be desired, or if a lower energy injection beam be provided, then a very different synchrotron architecture would be called for.

(We note that in the design assumption of 797-MeV H^- beam for injection, we have tied the design to LANSCE. However, we have provided an option for a 3-GeV booster synchrotron that can inject the same 50-GeV synchrotron. One of the purposes of this booster is to provide the injection beam at such other sites. For these other sites, an "inexpensive" lower-energy linac would be needed. It is clear that such a design will provide the necessary injection beam. Because of funding limitations of studies to date, the "inexpensive" linac option has not been fully developed, while a more explicit version of the booster is available.)

The next major assumption is that a maximum synchrotron fill of 3.3×10^{13} protons per cycle is sufficient to meet the radiographic requirements. A further implicit assumption is that the project will be staged in a way that a smaller fill will be sufficient during early operation, and that an operational period of several years will elapse before the synchrotron is required to routinely meet the maximum fill needs. For example, with a harmonic number of 1276 LANSCE bunches, 12 axes worth of beam (1×10^{11} protons per frame per axis delivered to the diffusers, with 26 frames and 12 axes, or 3.16×10^{11} total protons) can be provided including a small allowances for beam losses in extraction, beam splitters, etc. The maximum fill of 3.3×10^{13} protons per synchrotron cycle is simultaneously:

1. A judgment on the state of the art in high-energy proton synchrotrons.
2. A match to the capability of the LANSCE H^- linac (after an in-progress upgrade, the LANL Proton Storage Ring [PSR] will operate at 4.1×10^{11} protons per cycle with injection from a single LANSCE macropulse, including chopping losses for bunch-to-bucket transfer).
3. A cost issue (more protons will increase costs).

Our model for the synchrotron is the FNAL Main Injector, which is designed for 3×10^{11} protons per synchrotron cycle at 120 GeV. The Main Injector is expected to achieve this intensity without large phase space "dilution" after a few years of initial operation. "Proton Drivers" for neutrino production and/or sources for muon colliders at intensities on the order of 10^{11} or more protons per cycle are under consideration at other laboratories, but these require development beyond the present state-of-the-art. Incorporating such developments is beyond the scope of the studies so far undertaken. The reason for the assumption of slow development toward the maximum intensity is that no large margins in apertures and other hardware performance need be provided in order to assure that the synchrotron meets beam intensity requirements for initial operation.

The final assumption is that the six-dimensional phase space naturally available from a typical proton synchrotron is consistent with the radiographic requirements. There is no issue of a requirement on phase space to achieve the desired resolution. This occurs because the beam interaction with the diffuser and the object under test (multiple Coulomb scattering and straggling) results in an effective phase-space at the center of the object that is many times larger than the emittance of a typical synchrotron.

The main emittance issue is then to assure that the beam from the synchrotron fits in the aperture of the beam transport system at any stage in the development of the synchrotron. In particular, we need to be sure that the transport system is designed for the largest phase-space beam, which will be the beam at maximum intensity, including an allowance for phase space dilution. Finally, since the transport system has only a limited dp/p acceptance, it will be necessary to fix dp/p and show that the time spread of the pulse meets the radiographic requirements and does not degrade the performance of the extraction and pulse routing systems.

In the absence of compelling reasons driven by the physics requirements for changes in these "project design specifications" (50-GeV energy, either 797-MeV H^- injection or a 3-GeV booster for injection, 3.3×10^{13} protons per cycle, and that typical synchrotron emittance meets the requirements), the synchrotron design team has kept these constant for several years in order to allow steady progress towards a system design for AHF.

4.2. Pre-CDR Design

In the 1999 pre-CDR report (Ref. 5), a 50-GeV synchrotron design was provided. This design met all requirements. The particular features of this design included:

1. Use of existing FNAL B1 dipoles.
2. Injection energy of 797 MeV, extraction energy at 50 GeV.
3. Focusing-defocusing (FODO) lattice with a single length of dipole, transition gamma of 15.71.
4. 5-MHz RF, harmonic number 24.
5. Flexible extraction pattern, 200-ns minimum spacing, designed for synchronous transport layout.
6. "Full Aperture" abort system, 800-ns gap.
7. A space-charge intensity limit for 797-MeV injection of 0.5×10^{13} protons per cycle, 3-GeV booster required to reach 3.3×10^{11} protons per cycle.

The only unique item requiring development beyond the state-of-the-art in this system is the extraction kicker modulator. (Extraction with single pulse "cable modulator" requiring no new development meets most requirements.) A study of instabilities expected was included in the 1999 study. No problems were found. However, insufficient attention was paid to the issue of longitudinal phase-space blowup during crossing transition. Also, the issue of high peak power required to operate the magnet system was noted in 1999, but no effort was made to rectify this situation.

The conclusion of the 1999 study was that a synchrotron of this type was feasible. No show-stoppers were found. However, a number of issues were raised that required further study.

4.3. Issues Addressed in FY2000 Synchrotron Trade Study

The major thrust of the FY2000 synchrotron trade study was to consider options that might result in substantial project cost savings. At the start of the trade study, it was recognized that a change of the beam distribution system design from synchronous to asynchronous might have large cost impact. This change impacts the synchrotron through the extraction system, which must be able to provide beam pulses in a pattern that depends both on the layout of the beam distribution system and the pulse pattern on target required by the experiment. A further impact is the RF frequency of the synchrotron, which needs to be either 5 MHz or 10 MHz, depending on the pulse pattern scenario adopted, and also on the booster, which needs to deliver a beam appropriately formatted for a 5-MHz or 10-MHz synchrotron.

The second issue addressed was a study of the how to reduce power requirements (peak and average) while minimizing construction cost for the very low repetition rate needed for AHF. This study involves a tradeoff among power-supply costs, magnet-current ramp, magnet design (magnet coil cross section), power-distribution costs, and power-conditioning cost.

The third major issue addressed was a study of transition crossing in the synchrotron. Experience at other laboratories, e.g., European Center for Nuclear Research (CERN), FNAL, and BNL, shows that above some intensity, longitudinal beam motion becomes unstable for a short time during transition crossing. In this time, the longitudinal phase-space may blow up by a substantial factor. This blowup may be avoided by crossing transition quickly enough (by addition of a "gamma-t jump" scheme), or by other techniques. For example, by careful control of longitudinal parameters at transition crossing, there may be no blowup at all during transition crossing. (The FNAL Main Injector has successfully crossed transition at 90% of its design current without significant phase space blowup.) In the FY2000 trade study, we have studied the threshold for phase-space blowup in transition crossing, considered what it takes to provide for future addition of a "gamma-t jump" scheme, and have considered the design of a "transitionless" lattice that avoids the problem altogether.

The final major issue studied concerns the options for achieving the design goal of 3.3×10^{13} protons per accelerator cycle. In the pre-conceptual design report (pre-CDR), the transverse acceptance of the synchrotron was not large enough to accept this many protons during the injection process at 797 MeV. Thus the need for the inclusion of a 3-GeV booster in the project design. In the FY2000 trade study, we chose to consider what it would take to avoid a booster. Three approaches were considered, namely:

1. A lattice design with increased transverse acceptance in the same size dipole magnet,
2. Increasing the aperture of the dipoles and quadrupoles in the synchrotron, and

3. Raising the injection energy from the linac to 1.2 or 1.5 GeV, values being considered for some future LANSCE upgrades.

One less fundamental issue considered in the FY2000 trade study was the role of the existing FNAL B1 dipoles in AHF. In particular, we chose to evaluate the cost and technical impact of replacing these dipoles with dipoles of a different design.

4.4. Lattice Study

We chose to study five lattice types in the FY2000 synchrotron trade study. These were:

1. A pre-CDR type simple FODO lattice,
2. A superconducting magnet synchrotron,
3. A modified FODO lattice with provision for gamma-t jump,
4. A transitionless lattice, and
5. A triplet lattice.

We summarize the results of these lattice studies here.

4.4.1 Pre-CDR Type Simple FODO Lattice

The pre-CDR lattice was chosen to be as simple and straightforward as possible (see Ref. 5). It was based on a FODO type lattice with four long, dispersionless straight insertions. Magnets were assumed to be the existing FNAL B1 (main ring) dipoles, available in one length only. Dispersion matching was provided with 16 cells that have one (of two) dipoles missing. This was a simple lattice that could be constructed on a short construction schedule. However, the limitations of this lattice and the existing dipoles showed up in several ways. The limited aperture of the existing dipoles limits the number of protons available with 797 MeV injection to about 5×10^{11} protons per cycle, thus requiring the addition of a 3-GeV booster to reach full design intensity. The dynamic aperture in this design is marginal, a result of the poor field quality and sagitta of these (nearly straight) magnets. It is necessary to cross transition with this type of lattice, but a "gamma-t jump" scheme cannot be implemented with the type of dispersion-suppression scheme adopted. This scheme was made necessary by the use of a single length of dipole, as all the existing magnets are the same length. Finally, there are some reliability problems expected due to the 30-year age of the magnets and the design of the insulation in the existing coils.

Although none of the problems with this design alone is a show-stopper, the combination of issues raised is very serious. For this reason, we recommend no further study of the use of the existing Fermilab B1 dipoles.

4.4.2 Superconducting Magnet Lattice

We briefly studied the possible application of superconducting magnets to a 50-GeV synchrotron for AHF. We decided to shelve this idea, but save it for possible consideration should an increase in beam energy to ~100 GeV be considered.

4.4.3 Modified FODO Lattice with Provision for Gamma-t Jump

We considered minimal modifications to the pre-CDR lattice that would enable the future addition of a “gamma-t jump” system, allow use of new lower power consumption magnets of the type used in the FNAL Main Injector (MI) but properly bent to match the radius of 50-GeV protons, and some changes in the straight sections that better match them to the needs of the AHF injection, extraction, and abort systems. We found that with the proposed newly designed magnets, the dynamic aperture is much increased. We also found that a reasonable “gamma-t jump” system can be incorporated if, and only if, dispersion-suppression is accomplished with 16 cells containing two half-length magnets each. In addition, peak power consumption is much reduced, and injection, extraction, and a full-aperture abort can be accommodated within a circumference that is the same as the pre-CDR design. The space-charge limit for 797-MeV injection is $\sim 1.5 \times 10^{11}$ protons per cycle with a 2-in. (5-cm) gap magnet (as in the MI magnets). A second version, with 3-in. (7.5-cm) gap, was considered. In the 3-in. gap version, we can get to 3.3×10^{11} protons per cycle without need for a booster. Injection, extraction, and full-aperture abort can be accommodated in the 3-in. gap version, but only if we increase the circumference from $h=24$ (with respect to 200-ns bunch spacing) to $\sim h=26$. Power consumption is larger, but still reasonable, in the 3-in. gap version if magnets with larger coil cross section are adopted. The two versions of this lattice—2-in. gap with booster and 3-in. gap without booster—were chosen for costing in the FY2000 synchrotron trade study.

4.4.4 Transitionless Lattice

It is possible to design a lattice that avoids transition altogether. We studied such a lattice in the FY2000 trade study and found that it incorporates all of the beam dynamics properties required for AHF. The straight sections are essentially the same as in the lattice above, but were not studied in great detail. This lattice is a bit more complicated, requiring several lengths of quadrupole and six families of quadrupole power supplies. The circumference needs to be somewhat longer, but this was not studied in detail. Only a 2-in. gap version was studied, but we see no reason why a 3-in. gap version could not be developed. We have shelved this version because it appears to be more complicated and more expensive than the “gamma-t jump” lattice. It can quickly be adopted if problems with the “gamma-t jump” lattice are discovered.

4.4.5 Triplet Lattice

We studied a lattice in which the focussing is accomplished with quadrupole triplets rather than the doublets that make up FODO lattices. In this way, larger phase space can be accommodated with 2-in. gap dipoles, enough to avoid a booster for operation at 3.3×10^{13} protons per cycle with 797-MeV injection. The penalty for this type of lattice is that the quadrupoles must be approximately two times stronger than in a FODO, leading to a synchrotron that is somewhat longer. Extraction is a bit more difficult, but was not studied in detail. The biggest problem with this type of lattice is that a “gamma-t jump” scheme will not be possible, leading to a possible bottleneck in intensity at some time in the future. We have shelved this version in favor of the “gamma-t jump” lattice.

Table 2. Lattice Parameters for Reference Lattices

	2-in. gap	3-in. gap
Synch. Circumference (m)	1443.6 m	1563.9 m
(LANSCE Bunches)	1152 bunches	1248 bunches

	2-in. gap	3-in. gap
Betatron Tune	17.36 H / 17.44 V	17.36 H / 17.44 V
Number of Cells	68	68
Cell Length	1.23 m	23.00 m
Transition Gamma	14.18	14.16
Number of Dipoles	80/32	80/32
Dipole Length	6.783 m/3.3915 m	7.00 m/3.50 m
Dipole Field at 50 GeV	1.635 T	1.588 T
Number of Quadrupoles	13	136
Quadrupole length/ bore radius	1.295 m / 5.0 cm	1.75 m / 7.5 cm
Quad Gradient at 50 GeV	18.53 T/m	12.84 T/m
(Protons/Cycle, no Booster)	1.5×10^{11}	3.3×10^{11}

4.4.6 Lattice Study Conclusions

We have studied several lattices and have narrowed the selection down to one type with two magnet sizes, namely, a gamma-t jump conventional FODO lattice with either 2-in. or 3-in. dipole gap. The parameters of the lattices adopted are given in Table 2. The beam distribution system needs to be designed for the largest emittance expected from the synchrotron. Our six-dimensional particle tracking study is incomplete. We have therefore assumed a factor of 2 phase-space dilution in each of the two transverse planes and in the longitudinal plane. These are given in Table 3 below. Note that the phase space quoted in Table 2 is nominally "hard-edged," and must be fully transported in order to avoid beam losses. Also, the beam size due to transverse and longitudinal dimensions must be added "linearly," not "in quadrature."

Table 3. Beam Emittance of Synchrotron including Allowance for Phase-Space Dilution

	Transverse (normalized)	Longitudinal (5MHz)	Longitudinal (10 MHz)
2-in. Gap	56π mm-mrad	20 ns max x 100 MeV max 1.5 eV-s	10 ns max x 100 MeV max 0.75 eV-s
3-in. Gap	80π mm-mrad	20 ns max x 100 MeV max 1.5 eV-s	10 ns max x 100 MeV max 0.75 eV-s

We have chosen the 3-in. gap "gamma-t jump" lattice without booster as the reference design, with an option of using the 2-in. gap lattice with booster. It should be noted that even if the booster is not needed for 797 MeV, continued study of the booster is needed for application to sites at which 797-MeV injection is not available. We note also that the synchrotron circumference needs to be increased in the 2-in gap version if an asynchronous beam distribution system is adopted, and a further increase is needed if the 3-in. dipole gap option is adopted. This increase in circumference was not anticipated early enough in the year, so that it is inconsistent with the circumference used in the balance-of-plant study. This inconsistency needs to be resolved in a future study.

4.5. Synchrotron Magnet Study

One of the issues undertaken in the FY2000 synchrotron trade study was the relationship between the coil cross sectional area of the magnet coil and the lifetime cost of the magnet and its power system, including its power consumption. For our low-repetition-rate regime, we concluded that the dominant power system costs are related to the peak power demand of the magnet. By increasing the magnet coil cross-sectional area, which raises the magnet cost but lowers the power system cost, we reduce the peak power demand. A practical limit occurs when the dipole coil cross-sectional area (for 2-in. gap version) is about twice the area of the coil in the FNAL MI magnet. This large-coil was adopted for the 2-in.-gap dipole, and a scaled-up version of the same magnet cross section was adopted for the 3-in.-gap dipoles. A similar analysis was used to choose a quadrupole coil cross-sectional area. The results of the dipole magnet study are presented in Table 4 below. With injection at 797 MeV into a 50-GeV synchrotron with 16-kG peak field, the magnetic field at injection time is approximately 450 G. There will be a number of problems associated with the low injection-time magnetic field. These issues were beyond the limited scope of the FY2000 trade study and need to be resolved in future work.

Table 4. Peak Power Requirements for Synchrotron Dipoles Considered in Magnet Cross-Section Study

Magnet Type	Length	Max DC Power per Magnet (MW)	L/R (sec.)	Ramp Time (sec.)	Number Required	Peak Power Demand Total (MVA)
FNAL B 1 (1.5-in. gap)	All	0.135	1.08	3.0	104	15.4
MI-Like (2-in. gap)	Long	0.0656	2.57	5.0	80	7.4
	Short	0.0352	2.4	32		
Extra Copper (2-in. gap)	Long	0.0520	3.25	6.4	80	5.8
	Short	0.0279	3.03	32		
Extra Copper (3-in. gap)	Long	0.0727	5.01	9.8	80	8.2
	Short	0.040	4.55	32		

4.6. Magnet Requirements For Slow Ramp Waveform

We considered the issues that determine the desired magnet ramp waveform in the low-repetition-rate regime. When we optimize for the case of a magnet power system directly connected to the power grid ("direct drive"), we conclude that an exponentially rising pulse (constant applied voltage) is acceptable for the synchrotron beam dynamics. Costs of the power system decrease as the voltage applied to the magnets decreases, but average power consumption goes up. When we choose to have the magnet current reach the design current after a time on the order of $2 \times L/R$ (applied voltage = $1.1566 \times$ dc value), the total costs of the magnet, plus the power system, plus 10-years' worth of power consumption is minimized. The current waveform during the "down ramp" of the magnet system was briefly considered. Of course, since there is no beam in the synchrotron during the down ramp, there are no beam dynamics issues involved in this choice. The relevant issues are returning energy to the power grid, grid power transients, and repetition rate. If the magnet voltage is reversed during the down ramp, the magnet current will return to zero after a time on the order of $0.5 \times L/R$. If the voltage is set to zero, then the current will return close enough to zero after a time on the order of $4 \times L/R$. Reversing the magnet voltage during the down ramp maximizes grid impedance transients but reduces average power

consumption by on the order of 20%. Total pulse time (ignoring injection, flattop, and parabolas) is reduced from $6xL/R$ to $2.5xL/R$. If we were to choose the longer down ramp for the 3-in. gap dipoles, then the resulting total cycle time would be ~ 36 s. This could be reduced to 15 s if magnet voltage were reversed. Because neither power grid transients nor system tune-up was considered during the FY2000 synchrotron trade study, the issue of the magnet down ramp was left for resolution in a future year.

4.7. Pulse-Pattern Issues

The only identified physics requirement on the pulse pattern is for a number of consecutive pulses at small spacing. This requirement has never been precisely defined, and is interpreted somewhat differently in the community. Los Alamos has interpreted this requirement to be 10 consecutive frames, simultaneous on all axes within 50 ns, with 200-ns frame spacing. The number 10 is chosen to include the minimum number of pulses actually needed plus an allowance for "jitter," etc.

Although never formally set as a specific requirement, a sequence of "early" pulses will be necessary some experiments. All the time ranges specified in the requirements are longer than $1.8 \mu\text{s}$ (10 short pulses spaced by 200 ns), extending up to $75 \mu\text{s}$. Some specific reasons have been mentioned for requiring additional "early pulses" without clear definition of the number of early pulses or the pattern required. Indeed, flexibility of the pulse pattern is of the essence, as future experiments are not likely to be precisely defined at this time. We have interpreted the requirement for additional pulses in the following way:

- A string of 10 consecutive pulses (extracted on the last turn of beam in the synchrotron) with 200-ns spacing is an absolute requirement of highest priority.
- The option to have one pulse per turn (or skipped turns and/or a few pulses on selected turns) for up to $75 \mu\text{s}$ is a desirable goal of lower priority.

One metric of the extraction system/beam transport design is the number of additional pulses that can be provided. A better metric awaits a clearer definition of the requirement.

A synchronous beam delivery system, with all beam transport branches the same length (within the 50-ns pulse width tolerance), meets all the requirements and, with 5-MHz RF (200-ns pulse spacing in the synchrotron), maximizes the number of early pulses available. Asynchronous systems, with odd $\times 100$ -ns pathlength differences and a synchrotron with 10-MHz RF (100-ns pulse spacing in the synchrotron), give the same number of early pulses at lower cost. The drawback of this approach is that more demands are placed on the extraction kickers and modulators, and the design of the synchrotron and beam transport system become more tightly coupled.

The question studied in the synchrotron trade study was whether a choice of 100-ns pulse separation (10-MHz RF) is reasonable. The answer was that the beam dynamics, kickers, and abort system will be within the state-of-the-art. These will be of higher cost when compared with the 200-ns (5-MHz RF) version, and a first estimate of the cost differential is included in the appendices. A kicker modulator of the "single pulse" type, i.e., a modulator capable of extracting a single pulse from the synchrotron in any desired time sequence, is problematical if constructed using today's technology (if 100-ns pulse spacing is required). Such a modulator can be built and would have reasonable cost if 200-ns pulse spacing were chosen.

The conclusion we came to was that we should start operation of AHF at ~200-ns pulse spacing, but not preclude a future upgrade to ~100-ns pulse spacing if we choose an asynchronous system. Note that this conclusion is strongly dependent on our interpretation of the requirement, which is presently not very clear. It is possible to design an asynchronous system which is upgradeable from ~200-ns spacing to 100-ns spacing if, and only if, we properly choose the harmonic numbers (in terms of linac bunches) of the synchrotron circumference, the bunch length, and the path length difference in the beam transport system. We repeat that the choice of a synchronous system avoids altogether the need for such complicated harmonic matches. Synchronous systems decouple the transport system from the synchrotron and allow the use of any synchrotron bunch length that is a sub-harmonic of the synchrotron circulation time, with bunch length changes possible at any time. Further, the additional cost and risk of 100-ns kicker systems are eliminated by synchronous systems, which require only 200-ns kickers. However, it appears that synchronous beam distribution systems are more costly than asynchronous systems and the total project cost is minimized by such a choice.

Note that for the 2-in. gap synchrotron with asynchronous beam distribution system, and for the 3-in. gap synchrotron for all options, the circumference of the synchrotron does not match the circumference of the reference design (1152 LANSCE bunches) used in the balance-of-plant studies. This inconsistency must be removed in a future study.

A second question studied is the effect of the abort gap. We conclude that the abort gap makes only a small difference in the number of pulses available. If this is a problem, it can be corrected with a future upgrade. We choose initially an abort system with 400-ns risetime (400-ns abort gap). This is the version that is incorporated in our cost estimate.

The performance of our reference systems in terms of number of available pulses and pulse spacing is given in Table 5 below. Table 5 gives the pulse patterns available for reference systems as number of early pulses plus a string of 10 (or more) consecutive pulses. Limitations of initial operation include the choice of bunch spacing near 200 ns and cable modulator with limit of four (max.) early pulses and one long pulse, and 400-ns abort gap. After upgrade, we assume pulse spacing near 100 ns in the synchrotron, flexible single-pulse modulator, and 400-ns abort gap.

4.8. Beam Dynamics

4.8.1 Transverse Beam Dynamics.

First and foremost, we considered the issue of space-charge tune shift and the choice of injection energy. We considered the existing proton storage ring (PSR) at Los Alamos, which operates successfully with 797-MeV injection energy and an incoherent space-charge tune shift of 0.4. This was adopted as the upper limit of the allowed space-charge tune shift for AHF. We considered four possible injection energies for AHF, namely: 797 MeV, 1200 MeV, 1500 MeV, and 3 GeV. The 797 MeV injection energy assumes LANSCE H⁺ injection.

The 1200-MeV and 1500-MeV systems assume energy upgrades to LANSCE. Our conclusion is that for 2-in.-gap dipoles, only the 3-GeV booster option lowers the tune shift sufficiently to get below the space-charge limit with 3.3×10^{11} protons per cycle. For the 3-in.-gap option, 797-MeV injection meets our requirement. Thus, as far as AHF is concerned, there is no requirement for 1200 MeV or 1500 MeV injection in any case of interest. The 3-GeV booster is required only for

the 2-in.-gap case with 797-MeV injection, or for application at a site where no linac presently exists.

Second, transverse tracking with error fields and misalignments has been performed for all lattices and the 2-in.-gap dipoles. In addition, we also tracked the “gamma-t jump” lattice with 3-in.-gap dipoles. In all cases tracked, the dynamic aperture is larger than the physical aperture.

4.8.2 Longitudinal Beam Dynamics

We also started a study of longitudinal tracking in the synchrotron. Some longitudinal information comes from the pre-CDR study. This work was done with a 3-s linear magnet current ramp, so more RF voltage is required in the FY1999 study than is the case in the FY2000 study with exponential ramp, $2\pi L/R=11.8$ s. To date, the longitudinal tracking study (using ESME) has succeeded in transporting beam to 50 GeV with a linear magnet current ramp, crossing transition as required. Without a “gamma-t jump,” a factor of three dilution of longitudinal phase space is observed (exceeding the factor of two allowance we have built into the synchrotron design.) Possible remedies (in order of increasing cost) are:

1. Modifications to the RF amplitude/phase program to increase bunch length at transition time.
2. Compensation of the longitudinal impedance of the accelerator at transition time (using a variable inductor).
3. Increasing the rate of transition crossing with a “gamma-t jump” scheme (already designed).

4.8.3 Transition-Gamma-Jump Scheme

Figure 17 shows the transition crossing scheme using the gamma jump quadrupoles. The fast part of the jump is specified to last about 2 ms. The magnitude of the jump is $\delta\gamma = 1.5$. The pulsed quadrupoles have a strength of ± 5.1 T/m and a length of 0.348 m. Three jump quadrupoles are placed in each dispersion-matching cell, for a total of 24. Figures 18-20 show the effect of the pulsed quadrupoles on the lattice function and dispersion.

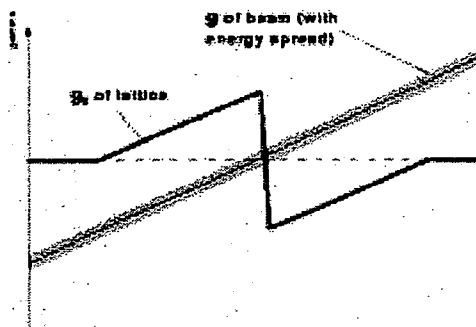


Figure 17. Transition crossing using pulsed quadrupoles.

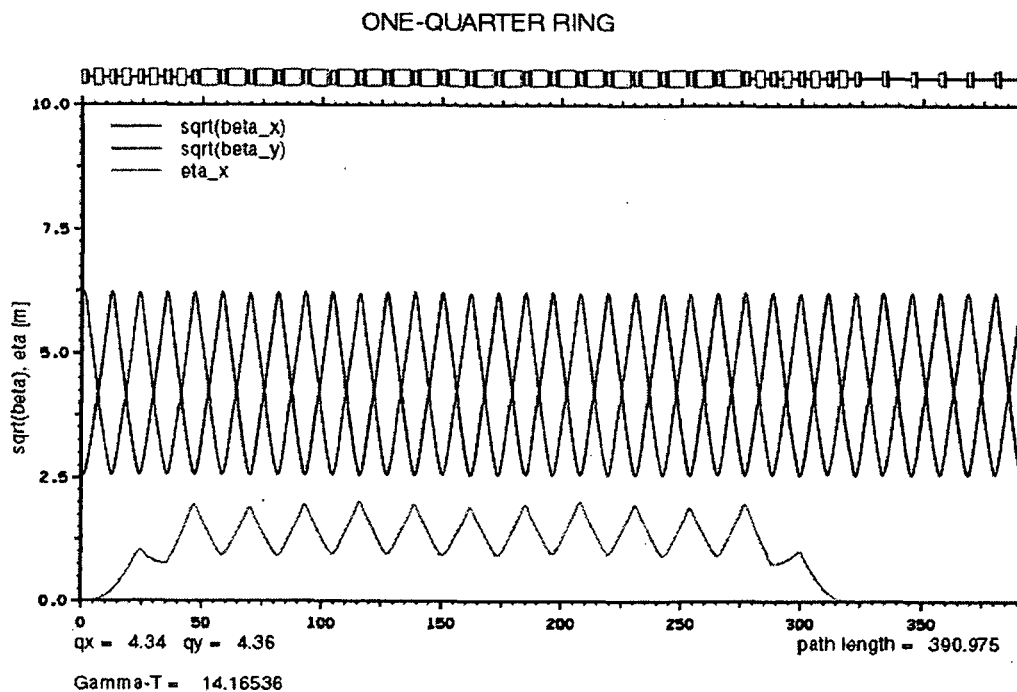


Figure 18. Dispersion and square roots of the beta functions plotted on the same scale. One-quarter of the 3-in ring shown for the nominal value of transition gamma.

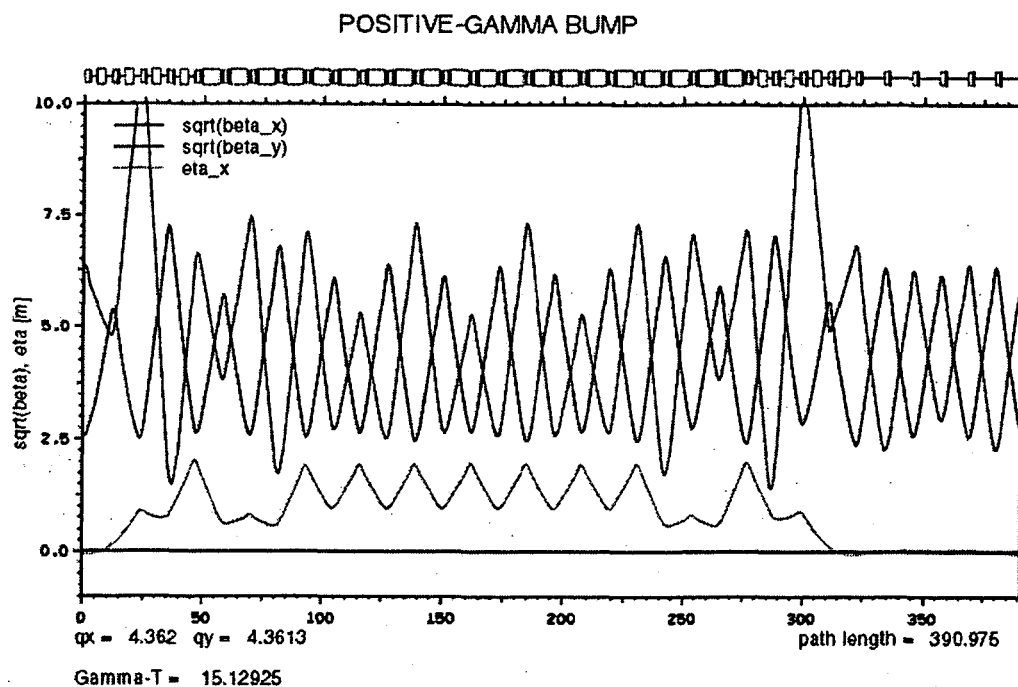


Figure 19. Dispersion and square roots of the beta functions plotted on the same scale. One-quarter of the 3-in. ring shown for the maximum value of transmission gamma, 15.13.

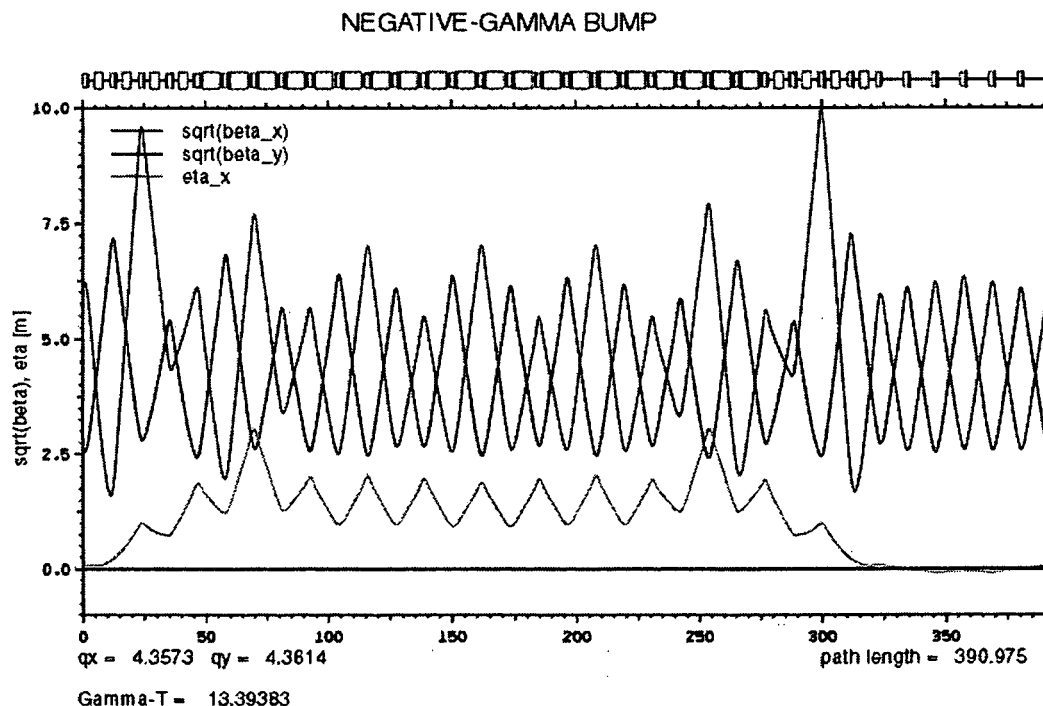


Figure 20. Dispersion and square roots of the beta functions plotted on the same scale. One-quarter of the 3-in ring shown for the minimum value of transition gamma, 13.39.

Table 5. Upgrade Paths from 200-ns Bunch Spacing to 100-ns Spacing

	2-in.-Gap Dipoles	3-in.-Gap Dipoles
Asynchronous, Superconducting		
Initial Operation ~5 MHz RF	4 early +12 consecutive (h=27, 177.8 ns spacing)	3 early +10 consecutive (h=23, 226.8 ns spacing)
After Upgrade ~10 MHz RF	12 early +10 consecutive (h=48, 200.6 ns spacing)	13 early +10 consecutive (h=54, 193.2 ns spacing)
Asynchronous, Normal-Conducting		
Initial Operation ~5 MHz RF	early +11 consecutive (h=27, 177.8 ns spacing)	early +10 consecutive (h=23, 226.8 ns spacing)
After Upgrade ~10 MHz RF	12 early +10 consecutive (h=48, 200.6 ns spacing)	13 early +10 consecutive (h=54, 193.2 ns spacing)
Synchronous		
Initial Operation ~5 MHz RF	early +18 consecutive (h=24, 200.6 ns spacing)	early +20 consecutive (h=26, 200.6 ns spacing)
After Upgrade ~5 MHz RF	13 early +10 consecutive (h=24, 200.6 ns spacing)	14 early + 10 consecutive (h=26, 200.6 ns spacing)

4.9. Extraction and Abort

4.9.1 Extraction-Section Layout

The layout of the extraction section is shown in Fig. 21. The figure represents the horizontal layout and beam envelopes for the 3-in.-gap reference ring. This is the most challenging case. The extraction system uses two 9-m-long, 50-ohm TEM kickers of a type used in existing machines, like the Los Alamos Proton Storage Ring. The envelope shown in Figure 21 assumes a push-pull voltage of 50 kV. A schematic representation of the kicker is given in Fig. 22. As shown in Fig. 21, the extraction system includes the two kickers, positioned symmetrically with respect to a focusing quadrupole, two Lambertson-type septa straddling a second focusing quad, followed by two C magnets. Except for the larger size, required for the 3-in.-gap case, the septa and C magnets are similar to the magnets described in the FNAL MI report.¹¹

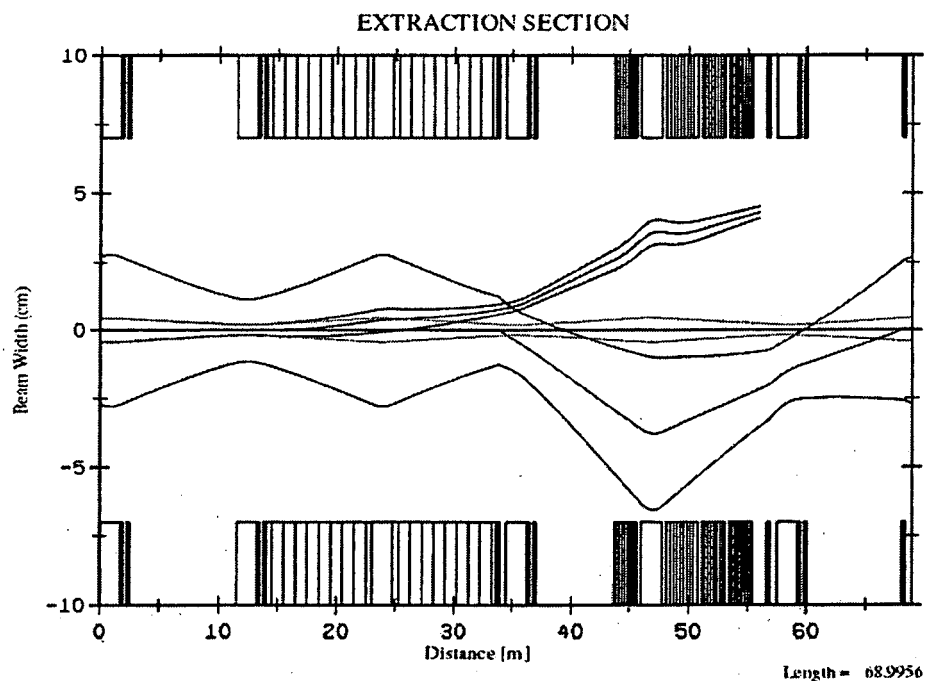


Figure 21. Extraction section for the 3-in. reference ring. Horizontal view. Shown are the envelopes of the large beam at injection, the beam after acceleration, after being bumped closer to the septa, and the extracted beam.

¹¹ Fermilab Main Injector, Technical Design Handbook, November 1995.

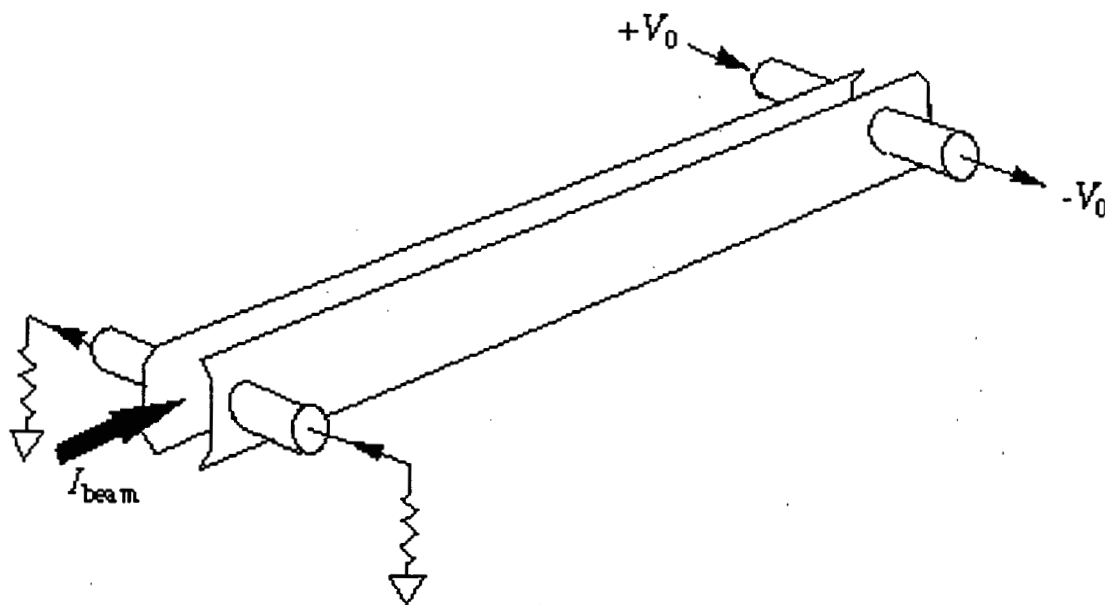


Figure 22. TEM kicker schematic. Note that the power is fed in the direction opposite the beam.

4.9.2 Kicker Modulators.

We studied the necessary kicker modulators for the reference 3-in.-gap and for the 2-in. gap gamma-t jump lattices. The kicker modulators were found to be reasonable, except for the “single pulse” 100-ns-gap modulator. We have adopted cable modulators for initial operation and reserve the flexible single-pulse modulator as an option for a future upgrade. Cable-type modulators for a single long pulse and four additional early pulses have been incorporated in our cost estimate. The flexible pulse-extraction upgrade would probably involve the use of stacked-FET modulator systems like the one shown in Figure 23.



Figure 23. Stacked-FET kicker modulator developed at LLNL.

5. Multi-Axis Imaging for Proton Radiography

5.1. Introduction

The AHF is planned as an important part of the U.S. Stockpile Stewardship Program to perform proton radiography, i.e., the observation of fast events by illumination with protons that are subsequently focused to provide an image of the events. In addition to a spatial image, an angular image is obtainable, using a special lens system that allows determination of the materials involved in the event.¹²

5.1.1 Radiography Requirements on The Transport System

In order to obtain a tomographic reconstruction of events, views from several directions are needed. The number of views desired is determined by the required resolution, assumptions about symmetry, and *a priori* knowledge of the events under observation. There are, of course, practical limitations on the number of views that can be implemented. At present, up to 12 views have been specified, requiring 12 beamlines converging on an interaction region.

Obtaining information on the time evolution of events requires several frames separated by from ~200 ns to several microseconds. A mixture of such framing sequences may be desirable for certain applications. Although pulse patterns do not originate with the transport lines, such timing considerations affect the beamline configuration and switching devices. A cycle rate of between 10 s and 100 s mainly affects the magnet cooling systems as well as the average power.

The transport configuration is also strongly influenced by the required beam energy, which has been specified at 50 GeV. This choice of energy is a compromise between increased imaging resolution and energy and cost of implementation. Since bending radii and quadrupole strengths are proportional to particle momentum, transport-system size and cost become awkward at energies much above 50 GeV.

An additional requirement of 3×10^{13} particles/cycle at an estimated 10^5 cycles/year affects beam transport in that the fractional beam loss should not result in substantial activation of the transport-line components. Beamline apertures, diagnostics, and alignment are parameters to adjust such loss. The peak current in the transport lines corresponding to the 3×10^{13} particles, divided among several pulses, does not result in significant space-charge effects.

Other requirements place complementary or additional constraints on other of the AHF systems; we mention only those that bear on the transport system.

5.1.2 Early Work on AHF and Motivation for Present Study

Efforts prior to late 1999 resulted in a preliminary concept for AHF with the basic requirements of eight equal-length transport lines and normal-conducting magnets.¹³ The concept is shown in

¹² 1. C. Thomas Mottershead and John D. Zumbro, "Magnetic Optics for Proton Radiography," Proceedings of the 1997 Particle Accelerator Conference, Vancouver, p. 1397 (1997).

¹³ P. Walstrom, F. Neri, T. Mottershead, E. Ferm, J. Tegtmeier, K. Jones, D. Webb, J. Edwards, L. Waters, R. Little, J. Lundberg, R. Schafer, M. Hinrichs, J. McGill, M. Schulze, D. Friesel, P. Schwandt, S. Cereghino, J. Sarracino,

Fig. 24. The LANSCE linac injects an 800-MeV chopped beam into the harmonic-24 synchrotron to produce 20 narrow bunches that are extracted at will into the transport system. As it progresses through the system, the beam is cut into eight equal parts by a series of splitters. Each part then converges on the object of interest, labeled FS2 (i.e., Firing Site 2) in Fig. 24, with all parts arriving simultaneously. Alternatively, just after the first split the two beam segments can be directed to a two-line firing site, FS1 in the figure.

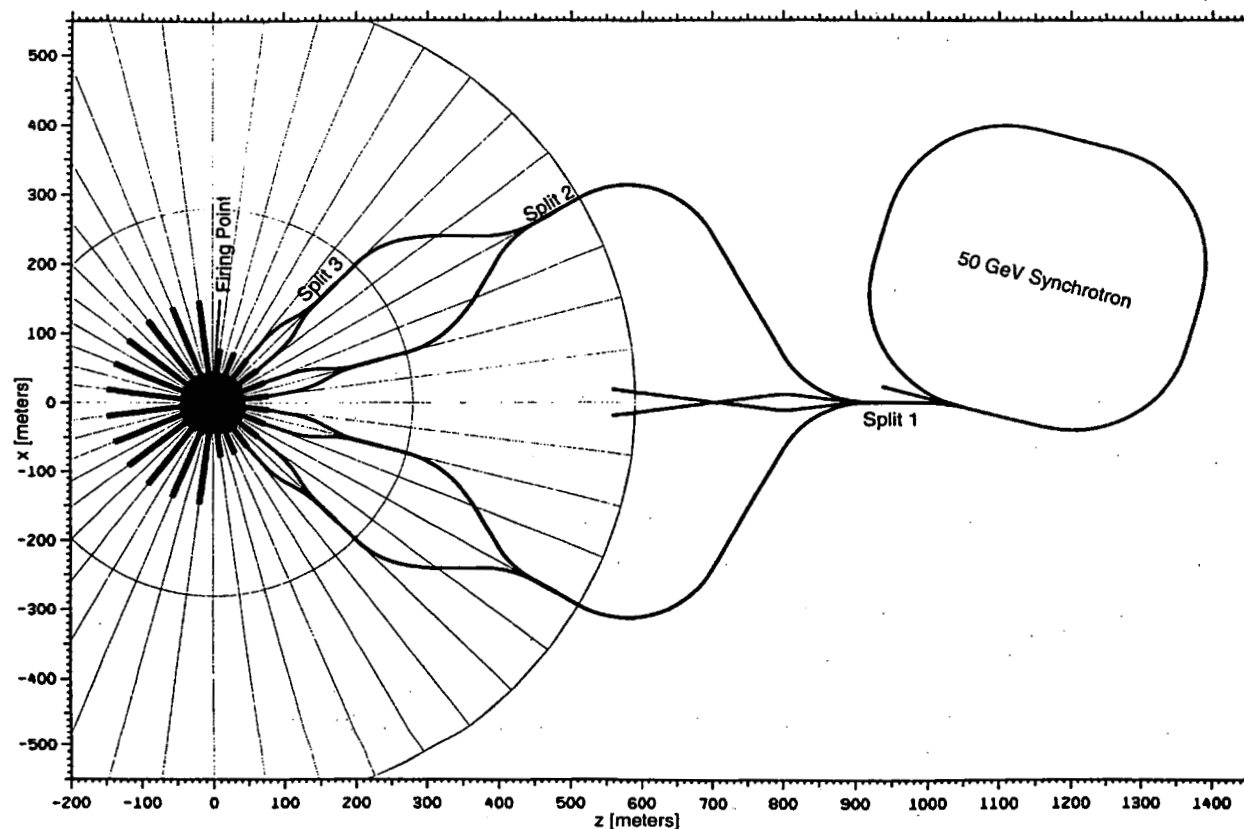


Figure 24. Early design of transport system, including lenses and synchrotron.

A recent study, described here, has gathered further requirements and proposed a number of options that were further detailed and the option tradeoffs evaluated. In particular, emphasis has been placed on minimizing power consumption and cost. Power is a special issue in both capital and operating costs since the peak power of the early design (up to 180 MW) would require extensive modifications to the power grid and/or large energy storage. Hence, superconducting magnets were to be considered, and configurations with optimal routing for fewer magnets were to be studied.

and A. Thiessen, "Draft Pre-Conceptual Design Report for the Advanced Hydrodynamics Facility," Los Alamos National Laboratory report LA-UR-99-4421 (October, 1999).

5.2. Methods of Approach

A team of several LANL physicists and engineers was involved in the study, some only a fraction of their time. Additionally, contracts to other institutions were established that supplemented the Los Alamos work, particularly in the area of costing and magnet design.

Along with interaction between designers and experimentalists to determine straw-man parameters, we first concentrated on variations of possible transport lines to minimize power and cost. Close interaction with the synchrotron design team was important for coordination of timing considerations and beam parameters. These interface considerations led to designs having two different line lengths to the object. These were called "asynchronous" as opposed to the "synchronous" cases first investigated. Having delineated a limited number of configurations involving various combinations of superconducting (SC) and normal-conducting (NC) schemes, modules for the various beamline functions were devised or taken from previous work and their beam-transport physics assessed. Lens configuration was also assessed and the most favorable variations selected for further study. Studies for cryoplant design and costing were also undertaken. Magnet design and contractor work assignment began as specifications and resources allowed. Contracts for the assessment of transport magnets were principally let with General Atomics.

5.3. Transport-Line Optimization

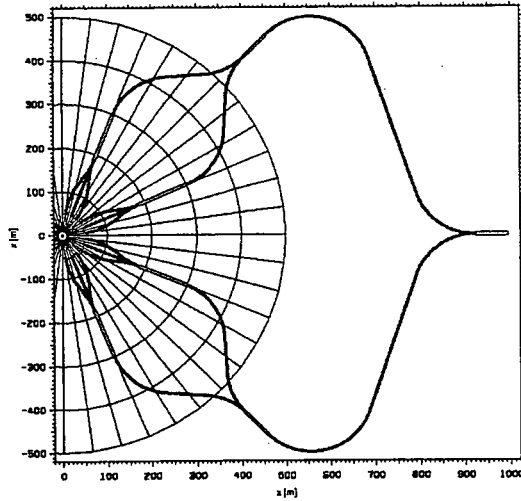
The simplest and most desirable method of providing 12 simultaneous pulses to the object is to have all paths to the target identical in length. Such a system is termed synchronous. The requirement of synchronicity leads to a longer total beamline length than the minimum lengths possible with designs for which the paths to the object have two different lengths, termed asynchronous designs.

We considered time differences between the two sets of lines that were a multiple of the ring-bucket interval, now decreased by a factor of two from the synchronous case. Thus, on a given frame, an initial pulse would be extracted from the ring to be shunted to the longer line by a "router" magnet (a resonantly driven ferrite deflector magnet operating at a frequency half the ring harmonic). A subsequent pulse would be picked out from the ring and shunted through the shorter line to arrive at the object simultaneously with the first pulse. It should be noted that for most pulse and timing patterns fewer pulses would be delivered from the ring with an asynchronous transport configuration.

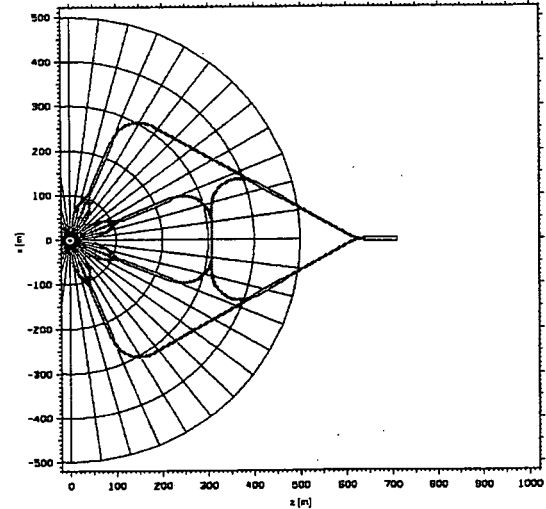
Ring design had set the bunch interval at 200 ns, but a 100-ns interval was considered possible, limited as a lower bound by the feasibility of the extraction-kicker risetime. Asynchronous designs were limited to an odd multiple of the 100-ns interval to maintain frame-interval versatility.

Specification of the pulse structure has undergone much discussion. Under consideration are the harmonic number of the ring, the ring period, and the transport-line time difference, which can be adjusted between about ± 100 ns with small effect on cost. The considerations couple the device feasibility—especially the ring extraction kicker—with pulse-sequencing feasibility and versatility as well as system upgradeability and kicker risetime. Specifically, ring harmonic number and line-length difference can be chosen such that a readily constructible ring kicker (with, say, a 200-ns risetime) could be initially used. When a faster kicker could be developed, an increase in the ring harmonic number would allow a greater number of pulses to be utilized. A

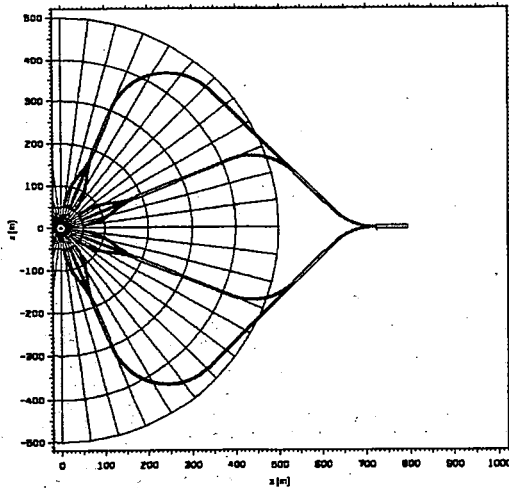
model has been constructed that assesses a cost for a restricted class of the infinitude of all options. It is believed that the restricted class encompasses all low-cost possibilities that meet system requirements. For each subclass—superconducting, normal-conducting, synchronous, and asynchronous—of the systems, the model chose a particular minimum-cost system. Many options still remained, especially combinations of superconducting and normal conducting, but four straw-man lattices were chosen for detailed study as adequately representative of all likely designs. These are pictured in Fig. 25.



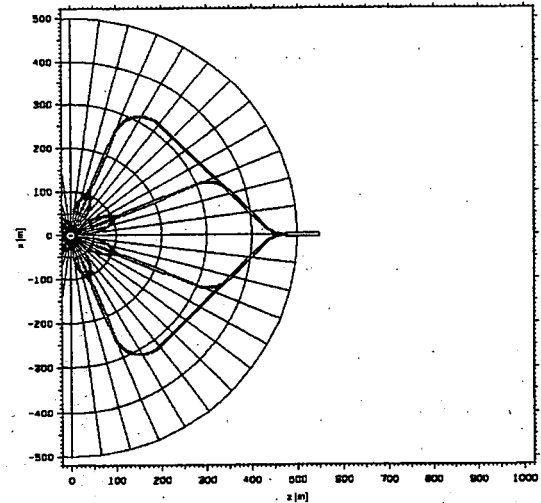
A. All normal-conducting synchronous.



B. All superconducting synchronous.



C. All normal-conducting asynchronous, with 900-ns time difference between outer and inner lines.



D. All superconducting asynchronous with 700-ns time difference between outer and inner lines.

Figure 25. The four straw-man designs selected for further analysis. All have been selected for minimum cost for their type within given constraints.

After matching to the first splitter, the general layout, as exemplified by the scenarios in Fig. 25, consists of the following:

1. A two-way split of each beam pulse into two symmetric lines.
2. A bend arc through an optimal angle.
3. Passage through a drift (including in some cases a bend) and match to a splitter.
4. A further two-way split, either by a static splitter or, in the case of asynchronous designs, dynamic deflection of alternate pulses by a pulsed kicker magnet. This provides four separated beamline branches.
5. Convergence on the target through a bend system.
6. Passage through a drift and matching to a third splitter.
7. Static splitting into three parts: One line from the first split leads straight to the target while the second leads to a further splitter. The two lines from this split curve away from the splitter into symmetric arcs that, by a further bend system, converge toward the object 15° from the straight line. The three lines span 30° with 45° between adjacent splitter straights. Thus 12 lines with equal synchronous pulses converge toward the object.
8. A lens complex. The four straight splitter lines direct the beam into four large field-of-view (30-cm) lens systems, while the eight arc lines direct beam into shorter high-gradient lens systems with a smaller field of view (12 cm). The 12 lenses span 165° , converging to a point at the object center and continue through the object. The lens magnets are all superconducting because of the high power needed.

The splitter sections for all scenarios are identical. The optimum beamlines after the third splitter (arc and straights in 7 and 8 above) are determined by the radius of the bend cell used and are hence identical for all superconducting scenarios and identical for all normal-conducting scenarios.

Designs for the splitters, bend modules, and transport from the third splitter to the lenses were nominally optimized and fixed. We then considered all possible design variations for four-branch systems. (Three-branch systems with nine object lines were also considered.) The problem can be formulated in terms of two bend angles for synchronous systems and one bend angle for asynchronous systems. Relative costs for straight-section transport, bend transport, tunnel, and splitter were assumed. These were based on last year's estimates as well as engineering experience. A program that iterated through all system angles was written and yielded minimum-cost designs for several types of configurations. The lens designs were not included and were regarded as of fixed length independent of the remainder of the system. The four representative designs shown in Fig. 25 were chosen from these results. Other possibilities that are near minimum in cost—i.e., within the uncertainty of the estimate—include mixtures of superconducting and normal-conducting sections as well as small variations of the asynchronous-lines time difference.

The designs in Fig. 25 are shown with scale. Note that the asynchronous designs are manifestly smaller in both footprint and line length than the synchronous ones. The superconducting designs are also smaller than the normal-conducting ones. The relative costs of the minimum-cost systems as determined by the formalism are

- normal-conducting synchronous: 1.0
- superconducting synchronous : -0.76
- normal-conducting asynchronous: -0.82
- superconducting asynchronous: -0.63

It is not surprising that the asynchronous designs were less expensive than the corresponding synchronous designs. It is, however, surprising that the superconducting designs actually cost less. This may be a consequence of the relative-cost factors used, but it encourages the consideration of superconducting options.

The recent cost estimate showed that, without the cryogenic systems, the relative costs of the four systems are close to those indicated above. If the cryogenic systems are included, the assessed relative costs are 1.0 (at \$208 million), 0.99, 0.80, and 0.90, respectively. A further iteration of the optimization may be desirable as higher-accuracy cost factors are determined.

5.4. Lattice Modules

The transport lattice can be divided into modules, some of which are used repeatedly throughout a given design. The concept of "matching" is important here. A particular module requires a given input beam to perform its function. In general, this is not provided by the upstream section, so an intermediate stage of focusing is needed. To perform arbitrary matching, a four-lens (quadruplet) system is needed and is used throughout the designs. In many cases, a triplet or doublet is adequate, particularly if it is convenient to restrict the beam-matching parameters by symmetry or other constraints.

A qualitative description of the important modules used in the designs is given below. An emittance of 40π -mm-mrad (normalized, $\sqrt{6}$ rms radius) was assumed in the design. However, all apertures have been assigned on the basis of twice this emittance with clearance for 4-rms radii and allowance for alignment and steering errors.

5.4.1 Transport from the Ring

The basic problem of the ring-to-transport-line interface is the optical and physical matching. A beam pulse is extracted from the ring by an electromagnetic kick that places the pulse in the deflecting region of a Lambertson septum magnet and thence through a vertical "C" magnet that further separates the extracted beam from the ring closed orbit. The end of the C magnet, including a further drift, defines the interface with the transport line.

At this interface, the beam enters a periodic FODO line with the same lattice period as the ring (21.2 m at the time of line design), to provide the optics match. The match is not exact due to unavoidable dimensional differences with the ring periodicity, but it is adequate. In the first half-cell, a pair of C magnets orients the beam horizontally. The following three cells bend the beam through 15° to interface alternatively with the FS1 firing site and with the line that leads to the FS2 transport. The bend is an achromat with the two end cells each containing two 3.75° dipoles. All magnets in this transport are normal-conducting, hence the design is the same for all scenarios. Although, the bend lattice is optically amenable to the use of the same superconducting magnets used in the FS2 superconducting designs, space and switching considerations made this infeasible. This interface is shown in Fig. 26.

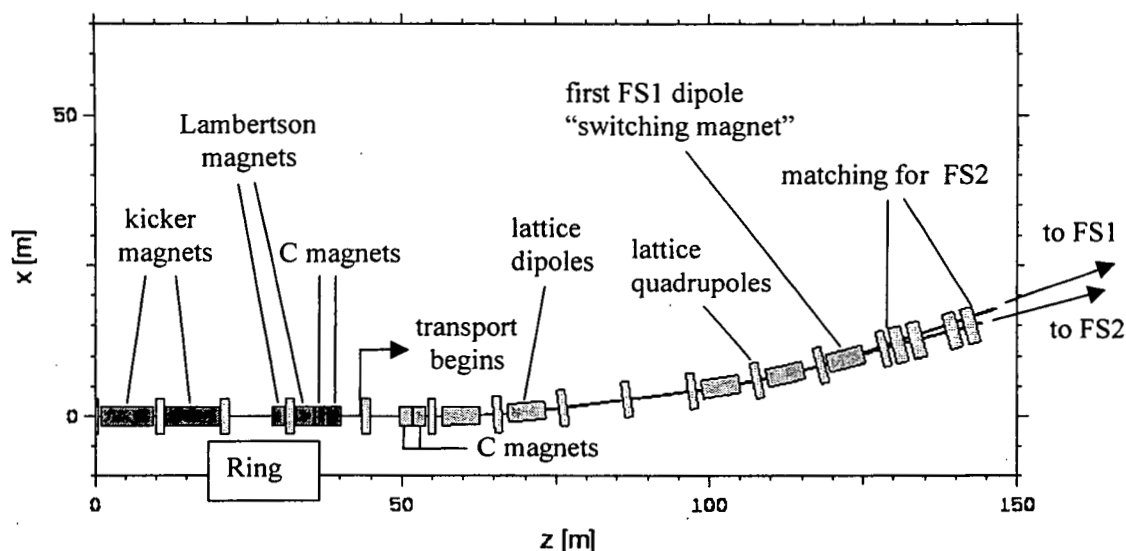


Figure 26. Beamline configuration near the ring/transport interface.

5.4.2 Transport to FS1

The earlier design specified two lines to a firing site located after the first splitter (cf. Fig. 24) to form a stereoscopic view of an object. The present design is simpler; a single-line site is placed after a further 15° bend that interfaces with and is identical to the bend from the ring. Alternative use of FS1 and FS2 is accomplished by activating or deactivating the first bend in the FS1 line.

5.4.3 Matching to the FS2 Transport-Spanning Long Drifts

The location of FS2 is specified to be at the center of Mortandad Canyon, an area some 900 m south of the LANSCE linac complex. Because of the varying size of the transport scenarios considered, the lengths of the lines leading to the first splitter vary from zero (for the entirely NC synchronous case that cannot be straightforwardly placed in the canyon center) to 350 m for the smaller asynchronous SC case.

Conventionally, such transport over long distances is done with a periodic lattice (FODO or doublet). Here, however, we considered the possibility of expanding the beam (to the extent that 3-in.-bore quadrupoles would not experience losses) to a negative correlation by means of a quadruplet configuration. The beam would drift through an intermediate waist symmetrically to an end point where it would be mirror demagnified to produce a beam matched to the next section. Using variations on this technique, it was possible, e.g., to bridge 50-m spans, without intermediate quadrupoles, and the span extended in 80-m intervals by a sequence of doublets. This is illustrated in Fig. 27, along with the transport to the lens along one path of the SC asynchronous case. As an alternative to a periodic line, fewer quadrupoles are used and larger spans without elements may provide economies in the tunnel construction or utilities. Use of the technique, in various forms appropriate to the situation, was not limited to matching to the first FS2 splitter but was generally used for matching through long spans in the remainder of the designs.

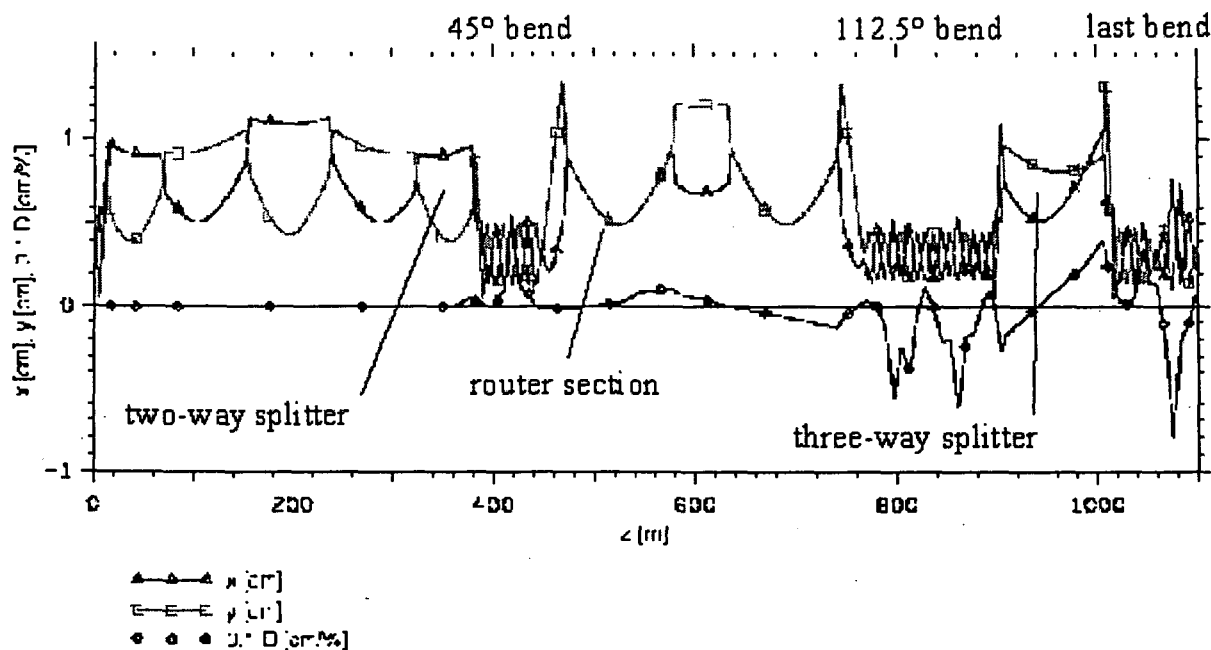


Figure 27. Beam envelopes for the outer lines of the SC asynchronous case (see Fig. 25-D).

5.4.4 Bend Modules

Each bend arc in the transport system consists of a periodic FODO lattice with the same generic cell repeated as required. The quadrupole strength varies with the bend-arc angle to make the arc achromatic. The bend modules discussed are nominal and are to be optimized for mechanical design and beam diagnostics and corrector placement in future designs.

1. **Normal-Conducting Bend Module.** The bend module used in the NC transport is shown in Fig. 28. The dimensions are magnetic lengths. Each cell bends 7.5° in 18.0 m with an average radius of curvature of 137.5 m.

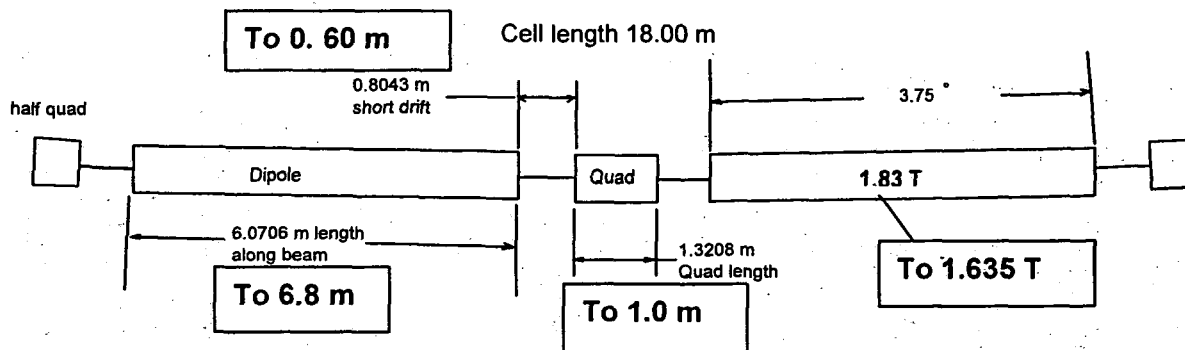


Figure 28. Normal-conducting bend cell.

2. **Superconducting Bend Module.** The superconducting bend module is shown in Fig. 29. The design is nominal since adjustments to mechanical, diagnostic, and cryostat requirements may require dimensional changes. A steering scheme has been worked out with superconducting steering magnets (occupying about 3 mm

of radial space) in the quadrupoles. Each cell bends 15° in 16 m with an average radius of 61 m. The magnet bend radius of 45.8 m is small compared to those of superconducting dipoles constructed for other projects. Beam-loss considerations require that the magnet be curved to this radius, a substantial consideration in magnet manufacture.

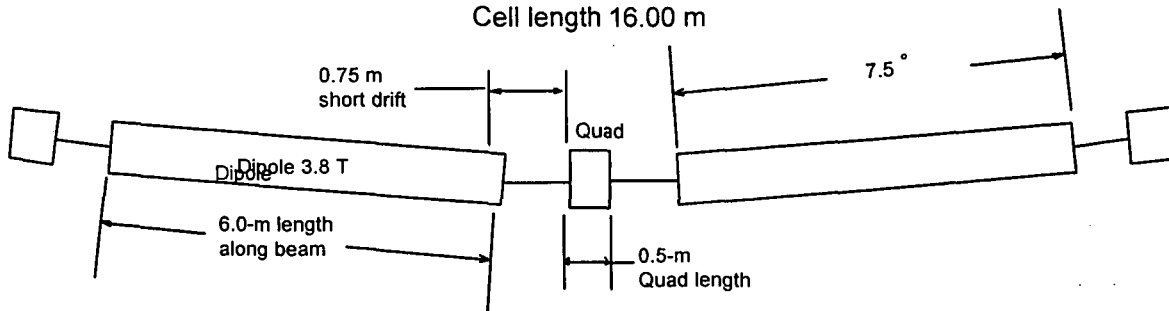


Figure 29. SC bend cell used in transport and magnetic design calculation.

5.4.5 Static Splitter

The static-splitter design is similar to that of the pre-CDR. The current splitter design is shown in Fig. 7. The electrostatic septum uses a wire grid with oppositely directed electric fields on each side to divide the beam and deflect each part of the beam by 0.21 mrad. A brief study shows only negligible heating of the wires by the beam (about 0.5% interception) at the highest beam repetition rate. The pulsed septum magnet further divides the barely separated beam using a 1.5-mm-thick septum and must have a duty cycle of less than 0.2 to remain thermally stable. Two further dc septum magnets are needed downstream to optimize total power. After another drift, the split beam halves are sufficiently separated to be captured by a pair of C magnets. The beams emerge from the final magnet pair ("H" magnets) parallel and separated by 1.06 m and are matched into the next transport section. Note that the split beams have lost their elliptical shape in phase space. A study showed that this effect is not noticeable on the object because of scattering by the lens diffuser.

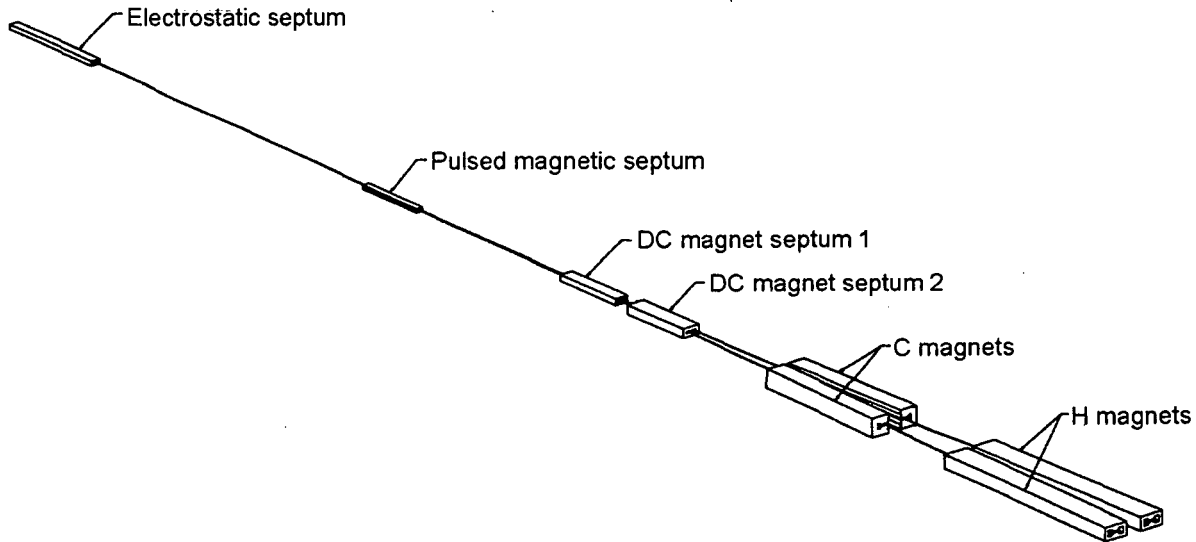


Figure 30. Isometric drawing (to scale) of a static splitter module. The module length is 41.0 m. For the dynamic splitter, the electrostatic septum is replaced by a router magnet and the first drift is lengthened.

5.4.6 Dynamic Splitter

The dynamic splitter is configured similarly to the static splitter and uses the same magnets, but the electrostatic septum is replaced by a resonant ferrite magnet (the “router”) that reverses sign every 100 ns. Thus, pulses that arrive at an odd multiple of 100 ns spacing are alternately shunted down the two beamlines after the dynamic splitter. The dimensions of this module differ somewhat from the static splitter for a total length of 69.5 m.

5.4.7 Three-Way (Static) Splitter

The three-way splitter, used as the final splitter, consists of two static splitters in series. However, the first splitter in the chain is rotated 90° so that the two beam halves are separated by 1.06 m vertically. The lower line then leads to a horizontal splitter that directs beam in two arcs to the lenses. The upper line forms the straight line leading to the lens but is brought to the level of the lower line by a pair of C magnets, identical to the splitter C magnets. Thus the lens lines are 0.53 m below the preceding transport plane.

5.5. Magnet Designs

Magnet parameters were specified by the optics requirements and magnet design was developed in collaboration with LANL’s outside contractor designers. A brief overview of magnet characteristics is provided here.

5.5.1 Lattice Magnets

The lattice magnets are the quadrupoles and dipoles that constitute the system bends. Since they are more numerous than other magnet types, cost and power considerations were important. Both SC and NC options were considered. Los Alamos and General Atomics contractors concentrated

on assessment of modified Relativistic Heavy-Ion Collider (RHIC) cold-iron magnets for the superconducting option. Questions as to the possible modification of the RHIC magnets to accommodate the large curvature needed in AHF were resolved by analysis of the coil stress. Further analysis is needed to determine whether the magnet coils can be wound straight and then distorted or must be wound on a curved mandrel to meet radius-of-curvature requirements.

The normal-conducting lattice magnets were designed to minimize power by increasing the copper content, somewhat at the expense of cost. DC-power consumption of the selected dipole magnet was 24 kW while the quadrupole powers ranged from 2.0 to 3.4 kW, depending on application. The dipole assessment was done as an alternative to the use of the FNAL B1 dipoles that required high powers and were marginal as to quality and beam-loss considerations. An example of a low-power dipole magnet design is shown in Fig. 31.

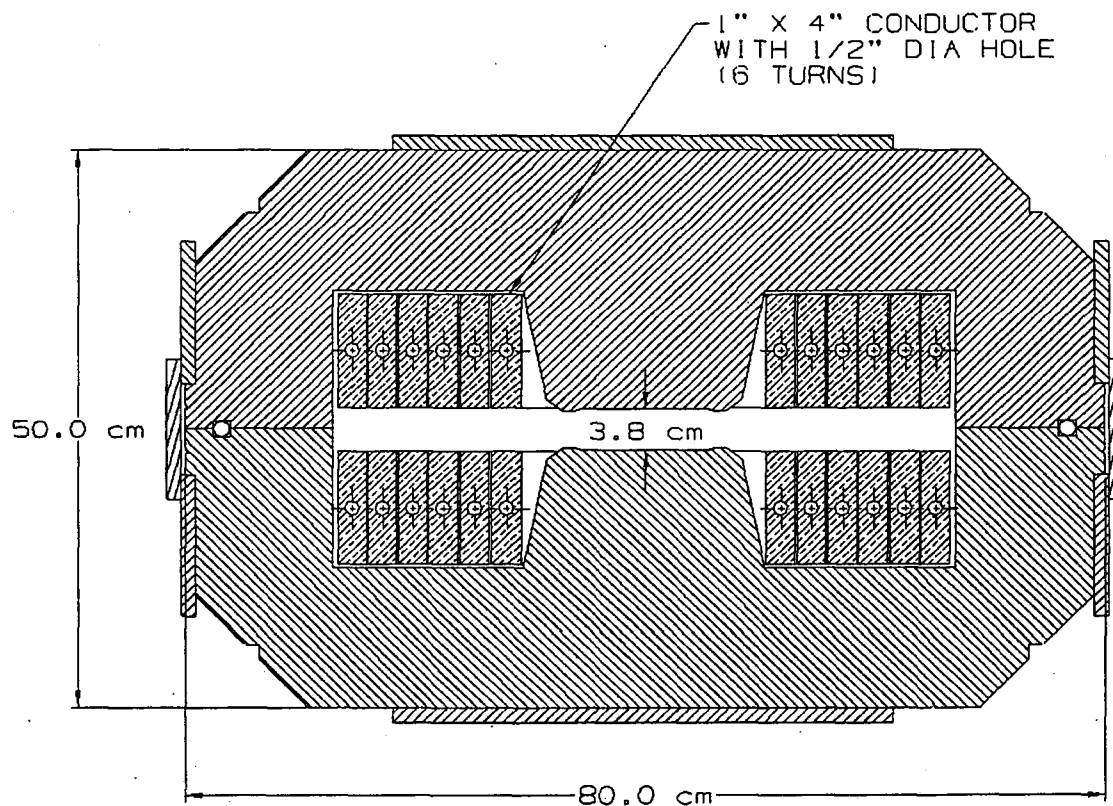


Figure 31. Low-power lattice dipole cross section.

5.5.2 Splitter Magnets

The five dipole-magnet types used in the splitter were designed to minimize power. The pulsed septum magnet has a thin septum separating the two beams. It requires a pulse less than 200 ms and will be pulsed with an energy-storage device to 9500 A with a peak power of 76 kW. The two septa require relatively high powers, totaling 470 kW peak for the pair because the narrow septa can contain a limited amount of copper. Each splitter requires 680 kW peak power and 215 kJ of energy per cycle.

5.5.3 Matching Magnets

The two types of 2-m-long matching quadrupoles (2-in. and 3-in. bores) were designed by Los Alamos to minimize power. Only normal-conducting magnets were considered, appropriate to the situation of varying strengths and scattered location throughout the facility. The average powers of the magnets were about 14 and 21 kW, respectively. The number of each type of magnet varied with scenario, but was typically 50 and 100, respectively.

5.6. Magnet Powers

To minimize power consumption, the magnets are operated in a pulsed mode. At cycle start a given magnet is brought to full current in twice the magnet time constant L/R , where L is the inductance and R is the resistance (magnet time constants range from 0.1 to 4 s). This implies a 16% overvoltage during the rise. Peak power is hence consumed at the end of the pulse rise. The magnets are then held at operating power for a time short compared to the rise to allow regulation and passage of the beam. Reversing the rise voltage then brings the magnet current to zero in 0.63 time constants.

A summary of power totals for the four baseline FS2 transport designs and the transport to FS 1 is given in Table 1. It is assumed that the magnet stored energy is returned to the line.

Table 6. Power Summary for the Baseline Designs

	Ave. P (kW) at 0.1 Hz	Peak P (kW)
NC asynchronous	3118	18172
NC synchronous	4334	21384
SC asynchronous	379	11454
SC synchronous	402	12208
FS1 transport	48	123

5.7. Cryogenic-Facility Design

A first-order design for the extensive facility needed to maintain superconducting magnets at cryogenic temperatures was performed. The magnet cooling required divides the AHF system into two areas: the lens superconducting magnets of FS2, which are cooled by pool-boiling helium, and the beam-transport superconducting magnets, located entirely in the bends, which are cooled by a flow of supercritical helium. Two systems are specified that separately cool the lens and bend magnets.

The lens system depends on a surface plant located above and to the north of the firing site. Supercritical helium is led to and around the firing-site-gallery circumference (33-m radius) for radial distribution to the lens lines. Each magnet cryostat contains a Joule-Thomson valve to produce two-phase helium at 4.35 K, and each lens line can be cooled independently with serial flow through the magnet string. Approximately 3.9 MW of wall power is required for the lens cryoplant to remove the 4.5 K equivalent load of 13.3 kW.

Because of the wide distribution of magnets, the bend-magnet system uses a distributed system of nine local cryoplants located in tunnel alcoves with a centralized compressor system. Although the bend arcs have varying heat loads, identical cryoplants, each with a 632-W equivalent heat-load capacity at 4.5 K, will be used. This permits a price reduction by the

purchase of multiple identical units. The system total wall power is 2.9 MW. Other options, including a central cryoplant, were assessed.

A cryosystem design for FS1 uses a similar underground cryoplant with surface compressor pumps. The 4.5-K equivalent heat load of 900 W requires 0.51 MW of wall power.

6. Magnetic Imaging Lenses for Proton Radiography

6.1. Introduction

In addition to the nuclear scattering, smaller-angle multiple-Coulomb scattering (MCS) of the protons also occurs in the test object and introduces a spread in the angles of the protons that are not nuclear scattered. In proton radiography, the blurring effect is almost eliminated by placing the detector at the focal place of a point-to-point magnetic quadrupole lens system. A second lens and detector system may be placed downstream of the first system. A third identity lens (the monitor lens) and detector are placed in front of the test object to record the incident beam intensity profile. Because the detectors are thin, a given proton passes through all of the detectors and is detected in all of them with almost unit probability. An additional large-bore quadrupole lens element is placed upstream of the monitor lens and test object to prepare the illuminating beam. In a single three-lens beamline, a total of 13 large-bore quadrupoles is required. In AHF, up to 12 converging beamlines will be used to make simultaneous images of the test object over a 180° range of view angles. Improved magnetic-optics performance and larger fields of view can be achieved by use of superconducting quadrupole magnets, which can produce higher pole-tip fields and gradients than conventional quadrupoles.

6.2. Magnetic Quadrupole Lens Optics

The basic identity lens used in proton radiography is a special quadruplet consisting of two identical cells, as shown in Fig. 32.¹⁴

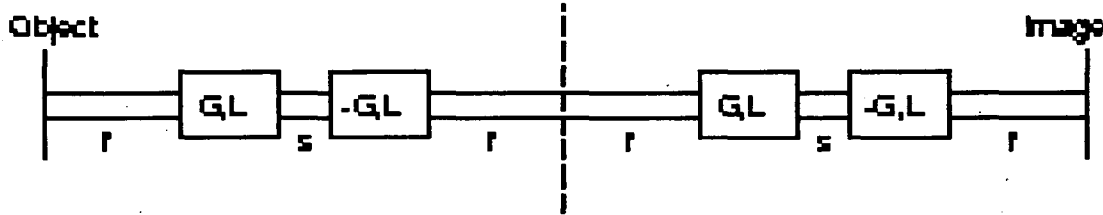


Figure 32. Configuration of identity lens.

This lens makes an inverted unit-magnification image of the test object in the image plane. Each cell is a symmetric doublet defined by four parameters: the focal standoff f , the interquad spacers, the gradient G , and length L of the four quadrupoles. Except for the alternating signs of the gradient, all four quadrupoles are identical. Because of the symmetry, the transfer matrix of this lens shows a remarkable simplicity. If the x -plane transfer matrix of one cell is

$$M = \begin{bmatrix} a & b \\ c & d \end{bmatrix} \quad (13)$$

then that of the two-cell lens is

$$R = M^2 = \begin{bmatrix} a\tau - 1 & -b\tau \\ c\tau & d\tau - 1 \end{bmatrix} = -I + \tau M, \quad (14)$$

¹⁴ C. T. Mottershead and J. D. Zumbro, "Magnetic Optics for Proton Radiography," Proc. 1997 Particle Accelerator Conference, Vancouver, B.C., May 1997, p. 1397 (IEEE Pub. 9CH36167).

where $\tau \equiv \text{Tr}(\mathbf{M}) = a + d$, is the trace of the matrix for one cell. To design an identity lens, we need only set the trace $\tau = 0$, leaving $\mathbf{R} = -\mathbf{I}$. (Note that the determinant = 1, always). Similar expressions apply to the y plane. Because of the symmetry, setting the x -plane trace to zero automatically sets the y -plane trace to zero, so only one of the four parameters is consumed in the process. The remaining three parameters remain free to be set by other considerations. In general, the focal standoff f is set by clearance requirements, and the interquad spacer s is set for engineering convenience, e.g. to fit both quads of the doublet in one cryostat. The gradient $G = B_0/(a+g)$ is determined by the quadrupole pole-tip field B_0 , the beam pipe inner radius a , and the radial distance g between the pipe inner radius and the pole-tip radius. For conventional iron-pole-piece electromagnets, a gap of $g \approx 1.5$ cm is reserved between the aperture radius a and the actual iron pole tip. In current-dominated superconducting quadrupoles, the pole-tip radius is defined to be the inner radius of the windings, and g is typically 5 cm. In conventional iron-pole-piece electromagnets, B_0 is limited by iron saturation effects to about 1.5 T. Considerably higher pole-tip fields can be achieved with the use of superconducting windings, the value being limited mainly by critical current limits of the superconductor, mechanical stresses, and cost. For a given focal standoff f and pole-tip field B_0 , the aperture radius a , and hence the quadrupole gradient G are determined by field-of-view requirements. (In this context, field-of-view refers to the transverse size of the largest object that can be imaged by the lens, with all protons that leave the object with less than a given angular spread passing through the lens system and not striking the inner radius of the beam pipe). The quadrupole length L may then be adjusted to focus the lens for 50-GeV protons. The process must be iterated for a large number of views N (typically $N = 12$), because the width of the quadrupoles depends on a , so the minimum standoff f needed to accommodate N views also depends on a .

All elements of the transport matrix (Eq. 14) are functions of the energy. The lens is in focus (i.e., $R_{12} = 0$) only for the particular proton energy for which $\tau = 0$. The chromatic aberration coefficients, which are the momentum derivatives of the R matrix elements evaluated at the nominal energy, express the fact that at other energies the lens is out of focus and does not have unit magnification. We define $\Delta \equiv \delta p/p$ to be the fractional deviation from the beam momentum for which the lens is in focus and denote the momentum derivatives of the R matrix elements with primes. In order to minimize chromatic effects, we illuminate the object with a correlated (laminar) beam in which the angle of the illuminating rays is a linear function of the distance from the axis, i.e., $\theta = wx$. If w is positive in the x plane, it is equal in magnitude and negative in the y plane. Such a strongly correlated beam appears to come from a (virtual) point source a distance $K = w^{-1}$ upstream of the lens. The choice $w = -R_{11}' / R_{12}'$ causes $R_{11}' + wR_{12}' = 0$. We call this "achromatic correlation" because, to first order in Δ , the final position of every proton in the beam that is not scattered from the illuminating ray trajectories is independent of its energy. The mission of the illuminator section in proton radiography is to prepare the incident beam so that only such "achromatic" rays illuminate the object (see Fig. 33).

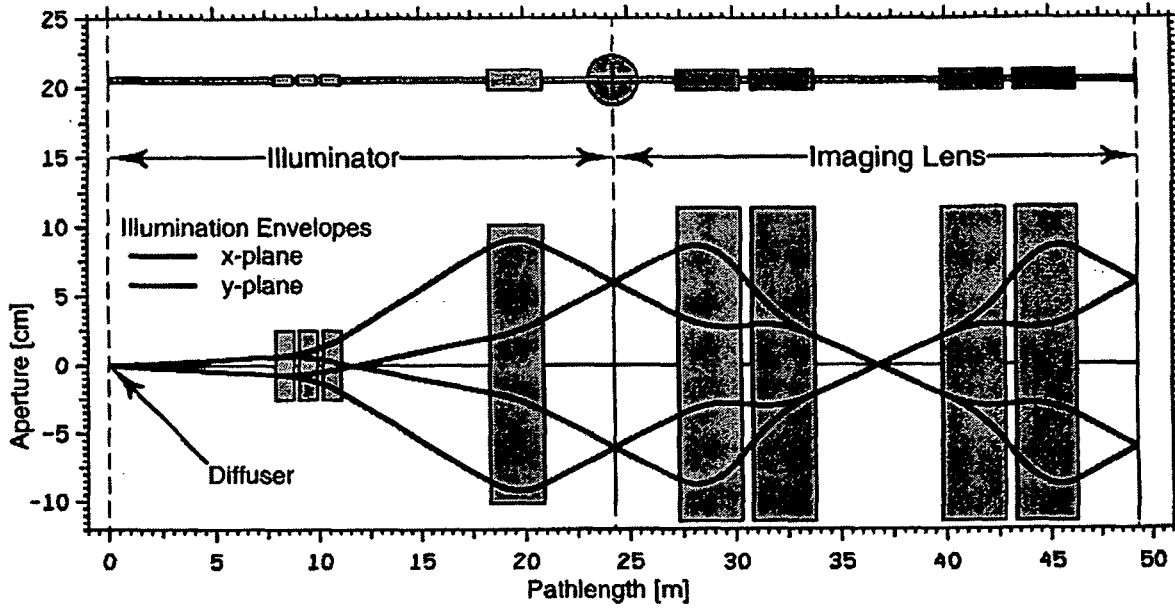


Figure 33. Schematic of illuminator lens and identity lens system, illustrating preparation of an achromatic illuminating beam. The shaded rectangles represent quadrupole magnets. The radiographed object is placed at the center between the illuminator and imaging lens.

The protons in such an illuminating beam exit the object and enter the lens with trajectory angle $\theta = wx + \phi$, where the scattering angle ϕ represents all deviations from the perfect correlation line due to both incident beam angular spread and scattering in the object. With $R_{12} = -1$, $R_{12} = 0$ at the nominal proton energy, the final position to lowest order is

$$x_f = -x + C_x \phi \Delta. \quad (15)$$

Here C_x is called the chromatic aberration coefficient of the lens. It is a measure of how much the off-momentum particles are out of focus. Particles with $\Delta = 0$ are in focus, meaning their final position is independent of scattering angle ϕ . Our aim is to make C_x as small as possible in order to minimize chromatic image blur, with a design goal of 30 meters or less. For example, if $C_x = 30$ meters, particles off momentum by + 0.1%, or $\Delta = 0.001$, or 50 MeV, come to a focus $C_x \Delta = 30$ mm past the image plane. Therefore, particles with $\Delta = 0.001$ and an angular deviation of, say, $\theta = 1$ milliradian from the illuminating rays would have an image-plane position shift of 0.03 mm.

Use of the achromatic illuminating rays in this particular lens leads to an additional important behavior that occurs at the midplane of the lens: that of angle sorting. That is, scattered protons with angle of the form $\theta = wx + \phi$ pass through the midplane at a distance x_{mid} from the axis that depends on their scattering angle ϕ , but not on their initial position, as shown in Fig. 34.

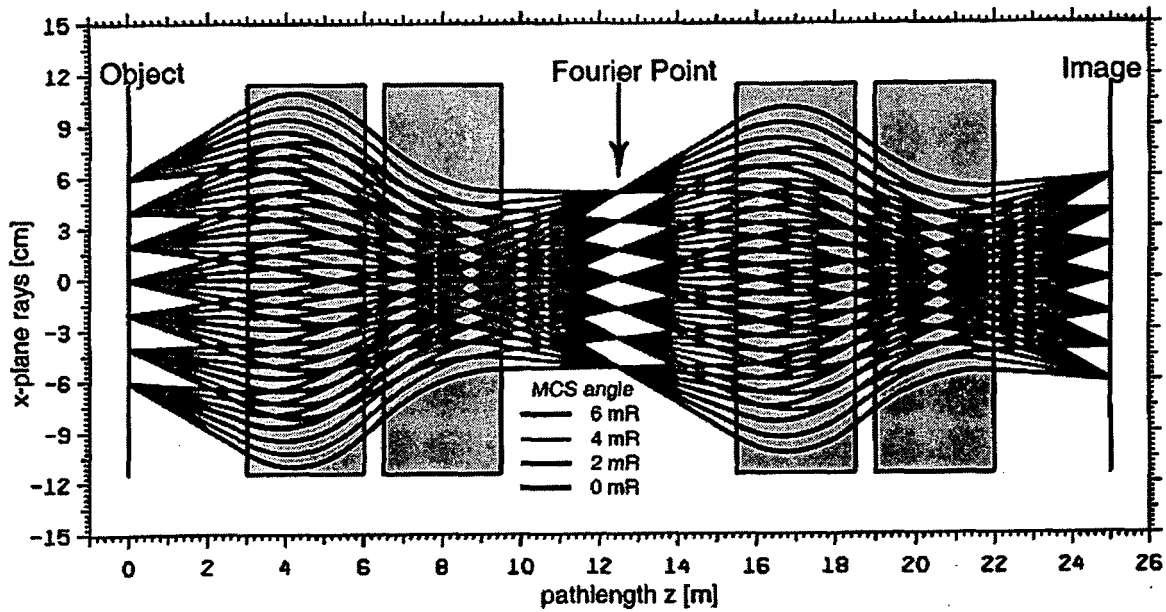


Figure 34. Illustration of midplane angle sorting with achromat illuminating rays in the identity lens.

Then, placement of collimators at the midplane allows cuts to be made on the scattering-angle distribution without introducing a large correlation between angle and position. In general, we want the smallest possible focal standoff f to reduce chromatic aberration, as well as overall system size. The practical lower limit for f is the larger of the limits given by containment-vessel size and mechanical interference between the outer envelopes of quadrupoles in adjacent beamlines. The presently used standoff distance of 3 m in AHF studies is determined by interference between quadrupoles. The quadrupole length L needed to focus a lens with given (f, s) depends on the quadrupole gradient G . Figure 35 shows the dependence of chromatic aberration on f for the three reference gradients.

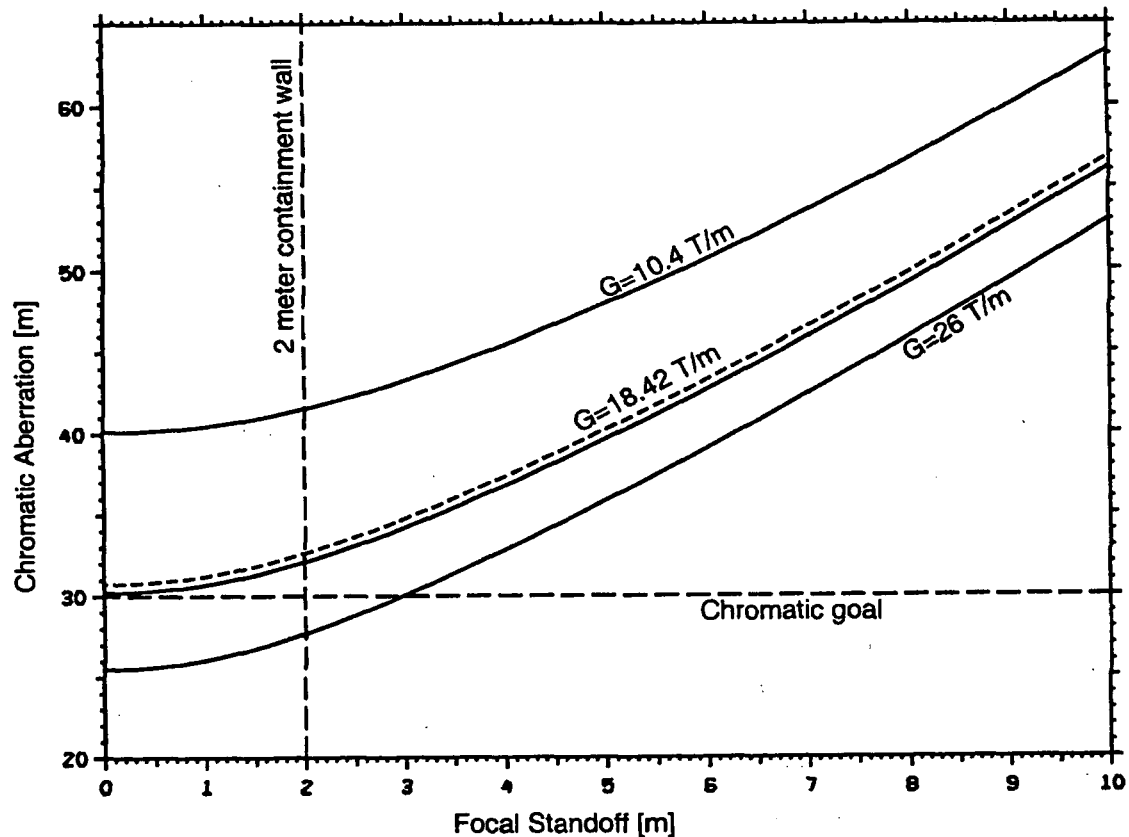


Figure 35. Dependence of chromatic aberration coefficient, C_x , on focal standoff, f , for various gradients.

The chromatic aberration of a lens depends on its overall length $L_{Tot} = 4f + 4L + 2s$, and so rises with increasing focal standoff. Note also that higher gradients lead to shorter quadrupoles, and lower chromatic aberration. The solid curves are for $s = 0.5$ m, the dashed curve for $s = 1.0$ m. The chromatic goal of $C_x = 30$ m is met only for the highest gradient, 26 T/m, with $f < 3$ m. Since technical difficulty, cost, and outer envelope dimensions for a quadrupole of a given inner bore diameter increase rapidly with gradient, a design with a lower, more realistic gradient (18.4 T/m) and somewhat larger chromatic coefficient (34 m) was chosen for the small-FOV quadrupole in the year 2000 AHF study. A still smaller gradient of 10.4 T/m and larger chromatic coefficient of 43 m were chosen for the large FOV quadrupole. However, because of its larger bore diameter, the lower-gradient large FOV quadrupole has about the same peak winding field as the small FOV quadrupole.

There are two requirement specifications for the field-of-view (see Fig. 36). The small-FOV lens must pass at least 7 mrad of scattering out to 6 cm off-axis. The large FOV lens must pass the same 7 mrad out to 15 cm off axis. The FOV of a lens is determined by the trajectories striking the inside of the beam pipe at the point of maximum excursion and is smaller than the beam-pipe diameter, since the trajectories diverge in some places (see Fig. 35). A rough rule of thumb is that the FOV diameter is about 2/3 of the beam-pipe diameter.

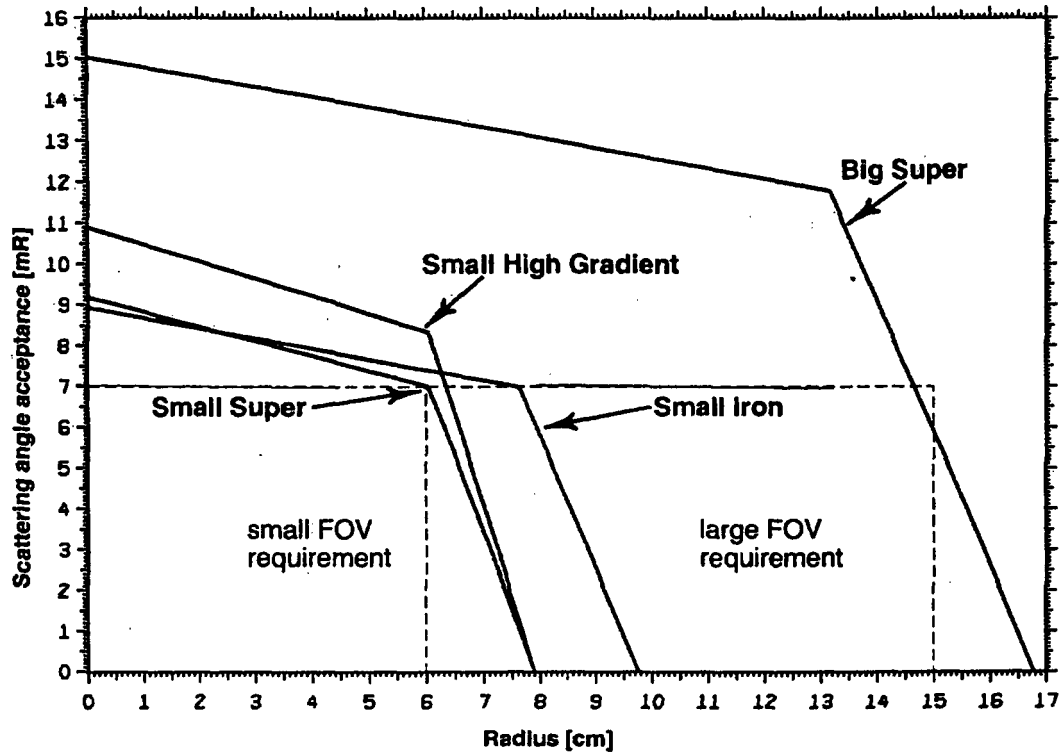


Figure 36. Field of view for four reference lenses. A given lens passes all protons with object-plane radius and angle that fall below and to the left of the curves. FOV requirements for the two nominal FOV cases are shown by the dashed rectangles.

6.3. The Quadrupole Design Study

In spring-summer 2000 several quadrupole types were studied. Although quadrupoles with the same gradient have the same linear optics, independent of transverse size, large-bore quadrupoles provide a larger FOV but have more geometric aberrations at the outside of the field of view. All lenses in the study were based on a 3-m standoff. The quadrupoles studied included four different 10 T/m quadrupoles with a length of 4.25 m and a fifth, high-gradient quadrupole magnet, as follows:

1. **A normal-conducting iron pole-piece conventional quadrupole, pulsed, with a 10-in. ID beam pipe.** It was recognized at the outset that conventional magnets of this size could not be used for the full set of 156 magnets in the 12-beamline system because of power-consumption considerations. However, they could have application in single-beamline firing sites, and in limited areas where superconducting magnets could not be used, etc.
2. **A liquid-nitrogen-cooled, iron pole-piece conventional quadrupole, pulsed, with a 10-in. ID warm beam pipe.** This approach can lower average power consumption, but requires either large reactive power for a short time, or large local capacitive energy storage.
3. **A superconducting 10 T/m quadrupole, with a 10-in. ID warm beam pipe, scaled from Jefferson Lab superferric Hall-C Q1 magnet.** The scaled magnet has a smaller

bore, greater length, the same pole-tip field, yoke and outer cryostat height greater than yoke width (General Atomics scaling and cost study, summer 2000).

4. **A superconducting 10 T/m quadrupole, with a 19-in. ID warm beam pipe (the nominal large-FOV magnet and Case II of the Massachusetts Institute of Technology [MIT] spring-summer 2000 study).**
5. **An 18.4 T/m, 9-in. ID warm beam pipe (the nominal small-FOV magnet and Case I of the MIT spring-summer 2000 study).**

To minimize cryogenic heat loads, two superconducting quadrupoles (a doublet) will be placed inside a single cryostat. The largest effort of the above options was put into Items 4 and 5, the MIT study. The MIT study included the following design and analysis tasks:¹⁵

1. A brief survey of applicable winding design and helium cooling approaches, e.g., cable-in-conduit, helium-wetted Rutherford cable, Nb₃Sn vs. NbTi, superfluid bath cooling, etc., and an explanation of the reasons for choosing a particular approach. High-current-density magnets are likely to be preferred for reasons of cost.
2. Pre-conceptual design of the quadrupole for the two cases, including
 - Magnetic field analysis, 2D and 3D.
 - Conductor configuration (dimensions, no. of strands, Cu:S/C ratio, void fraction, I_{op}/I_c , insulation scheme, etc.)
 - Winding pack configuration (racetrack coils, cos. 2 θ , etc.)
 - Structural support scheme, i.e., local conductor stresses, radial and tangential forces.
 - Thermal shields (briefly)
 - Helium supply manifolds (briefly)
 - Warm or cold iron yoke, if needed. The feasibility of yokeless designs with correctors was to be investigated by LANL.
 - Warm beam tube
 - Availability of space for correctors, if needed (need for and design of to be determined by LANL)
3. Stability analysis. Demonstrate by numerical or/or analytic calculations or by scaling from existing magnets that the magnet will achieve design performance. Since only a small portion of one of the 10-14 quadrupoles in a beamline will be subjected to nuclear heating, the magnet cost will be dominated by magnets that can be designed for negligible nuclear heating. Given this basic design, which does not take into account nuclear heating, briefly examine the effect of pulsed nuclear heating, according to data from future hadronic cascade simulations by LANL, as available. Preliminary

¹⁵ J. H. Schultz, R. J. Camille, C. Y. Gung, A. Radivinsky, B. Smith, R. J. Thome, J. V. Minervini, R. L. Myatt, P. L. Walstrom, and J. A. Waynert, "Superconducting Quadrupoles for Proton Radiography in the Advanced Hydrodynamics Facility," paper presented at the Applied Superconductivity Conference, Virginia Beach, Virginia, Sept. 17-22, 2000.

calculations by LANL indicate that this heating can be reduced by shielding to less than 1 millijoule per gram of conductor in the first 10 cm of winding of the first coil downstream of the test object. Heating in the rest of the magnet is smaller and negligible in the rest of the magnets in the lens system.

4. Preliminary stress analysis

- cooldown, Lorentz forces, analysis of local cable stresses.

5. Protection scheme and analysis

- maximum hot-spot temperature,
- thermal- stress issues, and
- quench voltages and their relation to the insulation scheme.

6. Estimate cryogenic system load requirements and specify operating current.

7. A cost estimate.

The performance requirements for the quadrupoles of the MIT study are listed in Table 7.

Table 7. Performance requirements for MIT Cases I and II.

Parameter	Case I	Case II
FOV (6 mrad)	14 cm	30 cm
Beam-Pipe ID	9 in.	19 in.
Warm-bore ID	11 in.	21 in.
Central Gradient	18.4 T/m	10.4 T/m
Magnetic length (one quadrupole)	2.90 m	4.25 m
Integral gradient (one quadrupole in doublet)	53.6T	43.8 T

It was assumed that the beam pipe would be an independently supported inner pipe connected to the containment vessel. The quadrupole doublet cryostat will have a warm bore with an inner diameter larger than the outer diameter of the beam pipe to provide for a radial gap to accommodate movement of the beam pipe during dynamic experiments. Supports for the beam pipe will be designed to minimize mechanical coupling between the beam pipe and the superconducting magnets and cryostat. A radial gap of between 0.25 in. to 0.5 in. between the two was assumed in this study.

The nominal pole-tip field (field at the inner winding radius computed as the product of the central gradient and the winding inner radius) for the Case I magnets is 3.3 T. The peak winding field is 4.9 T. For the Case I magnets of the study, MIT chose to use for the conductor the Superconducting Supercollider NbTi dipole cable. Sufficient quantities of this cable exist for use in prototype development. In the conductor for the MIT study, the cable is to be soldered into a copper channel. This concept provides both greater radial strength for an edge-wound conductor and additional stability for quench recovery. The cable in copper in channel operates at 4.3 K and the windings are cooled with two-phase helium. The windings are two-layer windings of the cos 2 θ type and are yokeless and collared with pre-compression.

The study examined designs with and without epoxy impregnation from the point of view of mechanical strength and stability against thermal loads. Stress analysis indicated that the potted

winding pack concept together with an external collar with pre-compression was a credible mechanical design approach and met all stress allowables for the materials.

Although the design was based on a yokeless concept in order to minimize interference between magnets nearest the firing point, addition of a warm iron shield or yoke outside of the cryostat where space permits is feasible. Use of a shield or yoke with a circular ID, as in typical accelerator ring magnets, adds relatively little to the quadrupole gradient (relatively more with low-field magnets, less with high-field magnets if saturation is minimized), but is desirable for field-quality reasons. Iron yokes or shields would have a circular inner diameter and an outside shape that would be rectangular, where space is limited, and circular, where available space is greater. The shield will be used wherever possible to reduce coupling (both of magnetic field errors and magnetic loads) between adjacent beamlines and nearby ferromagnetic structures. Since we may want to use our lenses at reduced beam energy (say, 25 GeV), use of superferrie magnets with highly saturated iron is undesirable.

The MIT magnets as designed can be protected from quench damage by use of an external energy dump with up to four quadrupoles in series.

In stability calculations, the largest expected heat input in the windings is pulsed nuclear heating by particles scattered from and produced in the test object. This has a significant effect only on those magnets immediately downstream of the test object. Recent MCNPX results for the small, high-gradient superconducting lens quadrupole show that without shielding at the inner radius of the magnet, peak energy deposition (2×10^{12} protons) will be about 0.35 mJ/g, which leads to a temperature rise of about 2 K. Designing for this relatively large heat input is possible, but it requires relatively expensive designs (use of NbSn superconductor instead of NbTi superconductor, etc.).¹⁶ Adding one inch of tungsten at the inner bore of the magnet, plus shielding at the end, reduces the peak and average heating by a factor of approximately four. With the shield, the design has enough margin in operating current over critical current (I_{op}/I_c) that the conductor temperature T reached just after beam pulses, as computed by nuclear heating codes, never exceeds the current-sharing temperature T_{cs} . Since the heating results came too late in the study to be incorporated into the final MIT design, the magnet size studied is based on the magnets without the shield. However, the unshielded magnets constitute 12 of the 13 large-bore magnets in a beamline. Therefore, the net cost impact of nuclear shielding on the overall lens system is expected to be small, but for the shielded magnets, the resultant increase in winding radius will presumably cause increase in peak winding field, stresses, and cryostat OD.

We may need to revisit the nuclear-heating results for the large-bore SC magnet (MIT Case II) because the earlier calculations for this larger magnet did not emphasize finite-object-size effects in computing nuclear heating.

A study of field-quality issues was begun at LANL in the summer 2000 study, but more work remains to be done. Preliminary tracking results indicate that a two-part specification is required. The field errors are specified at ID of beam pipe. The two-part specification includes a central-field error specification and an end-field error specification:

¹⁶ W. Lysenko. "Heating Effects," section 2.6.3 of "FY2000 Trade Study," Los Alamos National Laboratory report LA-CP-00-379, September 2000.

1. Central field: sum of absolute values of all error Fourier components to be no more than 0.001 of the quadrupole component.
2. End field: sum of absolute values of all error Fourier components, integrated through a single end region, to be no more than 0.001 of the GL product of the quadrupole.

These requirements can be met either by the quadrupole alone or by a quadrupole plus a system of correctors. The present MIT designs do not meet the end-field requirement (solving field-quality issues was not part of the MIT statement of work). It should also be noted that use of correctors may be cheaper than refining the quadrupole design with special end-turn shaping and spacing. Correctors may be needed in any case to correct geometrical aberrations and certainly will be needed to correct stray-field effects from yokeless quadrupoles in adjacent beamlines, if yokeless quadrupoles must be used to minimize mechanical interference. This is another subject for future study.

6.4. Conclusions

The basic quadrupole magnetic-optics concepts and requirements and design goals for proton radiography at 50 GeV in an AHF have been described. Cost-effective conceptual designs of superconducting quadrupoles that meet the basic AHF requirements have been demonstrated.